Mechanisms of sharp wave initiation and ripple generation

Schlingloff, D.[1, 3]; Káli, S.[1, 2]; Freund, T.F.[1, 2]; Hájos, N.[1], Gulyás, A.I.[1]

[1]Institute of Experimental Medicine, Hungarian Academy of Sciences, H-1083 Budapest, Hungary
[2]Faculty of Information Technology, Pázmány Péter Catholic University, H-1083, Budapest, Hungary
[3]János Szentágothai PhD Program of Semmelweis University, Budapest, Hungary
Abbreviated title: Organization of sharp wave-ripples

Abstract

Replay of neuronal activity during hippocampal sharp wave-ripples (SWRs) is essential in memory formation. To understand the mechanisms underlying the initiation of irregularly occurring SWRs and the generation of periodic ripples, we selectively manipulated different components of the CA3 network in mouse hippocampal slices.
We recorded excitatory and inhibitory postsynaptic currents to examine the build-up of neuronal activity preceding SWRs, and analyzed the distribution of time intervals between subsequent SWR events. Our results suggest that SWRs are initiated through a combined refractory and stochastic mechanism. SWRs initiate when firing in a set of spontaneously active pyramidal cells triggers a gradual, exponential build-up of activity in the recurrent CA3 network. We showed that this tonic excitatory envelop drives reciprocally connected parvalbumin-positive basket cells, which start ripple-frequency spiking that is phase-locked through reciprocal inhibition. The synchronized GABAA receptor-mediated currents give rise to a major component of the ripple-frequency oscillation in the local field potential, and organize the phase-locked spiking of pyramidal cells. Optogenetic stimulation of parvalbumin-positive cells evoked full SWRs and excitatory postsynaptic current sequences in pyramidal cells. Even with excitation blocked tonic driving of parvalbumin-positive cells evoked ripple oscillations. Conversely, optogenetic silencing of parvalbumin-positive cells interrupted the SWRs or inhibited their occurrence. Local drug applications and modeling experiments confirmed that the activity of parvalbumin-positive perisomatic inhibitory neurons is both necessary and sufficient for ripple-frequency current and rhythm generation. These interneurons are thus essential in organizing pyramidal cell activity not only during gamma oscillation, but, in a different configuration, during SWRs.

Introduction

Different types of behavior are accompanied by distinct brain states, which are characterized by various EEG patterns that indicate unique underlying network dynamics. Hippocampal sharp wave-ripple complexes (SWRs) occur during behavioral immobility and non-REM sleep (Buzsáki et al., 1983; Buzsáki, 1986) and consist of an aperiodically occurring field potential transient, the sharp wave, and a superimposed fast, periodic (150-200 Hz) oscillation, the ripples. SWRs were proposed to play an important role in memory consolidation (Buzsáki, 1989). Indeed, during SWRs information captured during previous exploratory behavior is replayed (Nádasdy et al., 1999; Foster and Wilson, 2006; Diba and Buzsáki, 2007) in a time-compressed manner, and the interaction between the hippocampus and neocortical cell assemblies results in the stabilization of memory traces (Wiltgen et al., 2004). Selective disruption of SWRs (Girardeau et al., 2009) causes memory deficits in hippocampus-dependent memory tasks.

In vivo and in vitro studies (Nádasdy et al., 1999; Csicsvari et al., 2000; Maier et al., 2003; Klausberger et al., 2003, 2004, 2005; Lasztóczi et al., 2011; Lapray et al., 2012; Hájos et al., 2013) revealed the behavior of principal cells and different subtypes of inhibitory neurons during SWRs and analyzed extracellular and intracellular currents. It was proposed that the strong recurrent collateral system of pyramidal cells (PCs) in CA3 enables this region to

initiate SWRs (Buzsáki and Chrobak, 1995; Csicsvari et al., 2000), which are then transmitted to CA1 via the Schaffer collaterals (Csicsvari et al., 2000; Ellender et al., 2010). However, most of the results to date derive from the CA1 area and are descriptive, found only correlations, but did not reveal mechanisms or causal relations. In particular, the following important questions remain open: How are the irregularly occurring SWRs initiated and shaped in the CA3 area? What are the current and rhythm generating mechanisms of the periodic ripple oscillations? To answer these questions, we developed an in vitro model system (Hájos et al., 2009) which allows rapid pharmacological interventions, local drug applications and the parallel measurement of network and cellular activity during spontaneous SWRs in the CA3 area of the mouse hippocampus.

Materials and Methods

Animals were kept and used according to the regulations of the European Community's Council Directive of 24 November, 1986 (86/609/EEC), and experimental procedures were reviewed and approved by the Animal Welfare Committee of the Institute of Experimental Medicine, Hungarian Academy of Sciences, Budapest. CD1 or C57Bl/6J mice of both sexes (postnatal day 17–29) were used in most of the experiments unless it is specified otherwise. SWRs with similar characteristics can be recorded form from both ventral and dorsal slices and also from slices prepared from older animas (we recorded from slices of up to 250 days old animals).

Transgenic animals. Transgenic mouse strain was used to selectively obtain recordings from perisomatic inhibitory cells. parvalbumin-positive (PV+) cells (PVBCs and axo-axonic cells) were sampled in a strain where enhanced green fluorescent protein (EGFP) expression was controlled by the PV promoter (Meyer et al., 2002). For optogenetic stimulation of PV+ cells the B6;129S-Gt(ROSA)26Sortm32(CAG-COP4*H134R/EYFP)Hze/J" (The Jackson Laboratory; RRID:IMSR_JAX:012569) strain was crossed with "B6;129P2-Pvalbtm1(cre)Arbr/J"(The Jackson Laboratory; RRID:IMSR_JAX:008069) animals to generate mice which selectively express channelrhodposin-2 (ChR2) under the PV promoter. A white light-emitting diode (3 mW) was used to illuminate (whole) slices from below. In contrast to other experiments, here we used older animals (postnatal day 60-300) due to low expression of ChR2-EYFP before this age. SWRs were spontaneously generated in these slices with similar properties as observed in young animals. In control animals, no changes were detected in response to illumination. Transfection: To selectively express eNpHR 3.0 PV+ cells, B6;129P2-Pvalbtm1(cre)Arbr/J"(The Jackson Laboratory; RID:IMSR_JAX:008069) animals was stereotaxically injected with pAAV-Ef1a-DIO eNpHR 3.0-EYFP (Penn Vector Core). The following coordinates were used (in mm): -2.6 anterior-posterior, ±2.5 and ±3.1 medial-lateral, −2.1 and -2.5 dorsal-ventral, 50 nl each). After 2-3 weeks following injection, horizontal or coronal slices were prepared as described below. A compact diode laser (640 nm; TOPTICA Photonics AG) was used for illumination. We quantified the accuracy of NpHR 3.0 expression in PV-positive neurons, and counted the number of cells expressing the two signals in CA3 area of 3 animals. We found that 71.5 % (198 of 277 cells) of PV cells expressed NpHR 3.0 in their membranes. We did not find NpHR 3.0 positive cells without PV immunoreactivity.

Slice preparation and recording conditions. In all cases, the mice were decapitated under deep isoflurane anesthesia. The brain was removed into ice-cold cutting solution, which had been bubbled with 95% O_2-5% CO_2 (carbogen gas) for at least 30 min before use. The cutting solution contained the following (in mM): 205 sucrose, 2.5 KCl, 26 $NaHCO_3$, 0.5 $CaCl_2$, 5 $MgCl_2$, 1.25 NaH_2PO_4, 10 glucose, saturated with 95% O_2-5% CO_2. Horizontal hippocampal slices of 300–600 μm thickness were cut using a vibratome (Leica VT1000S or VT1200S). After acute slice preparation the slices were placed into an interface-type holding chamber for recovery. This chamber contained standard ACSF at 35°C that gradually cooled down to room temperature. The ACSF had the following composition (in mM): 126 NaCl, 2.5 KCl, 26 $NaHCO_3$, 2 $CaCl_2$, 2 $MgCl_2$, 1.25 NaH_2PO_4, 10 glucose, saturated with 95% O_2-5% CO_2. The composition of the modified ACSF (mACSF) used in experiment presented in Figure 2F-G was the following (in mM): 126 NaCl, 3.5 KCl, 26 $NaHCO_3$, 1.6 $CaCl_2$, 1.2 $MgCl_2$, 1.25 NaH_2PO_4, 10 glucose saturated with 95% O_2-5% CO_2. After incubation for at least 1.5 h slices were transferred individually into a submerged-style recording chamber equipped with a dual superfusion system for improved metabolic supply to the slices (Hájos et al., 2009). In this design, the slices were placed on a metal mesh and two separate fluid inlets allowed ACSF to flow both above and below the slices with a rate of 3–3.5 ml/min for each flow channel at 30–32°C (Supertech Instruments; www.super-tech.eu).

Standard patch electrodes were used in all recording configurations (i.e., in whole-cell patch-clamp, loose-patch, and for field potential recordings). Pipette resistances were 3–6 MΩ when filled either with the intracellular solution or with ACSF. ACSF filled pipettes were used for local field potential (LFP) recordings and loose-patch recordings of firing patterns. After recording

the action potentials, the pipette was withdrawn from the slice and the same cell was re-patched and filled with a new pipette containing intracellular solution.

The composition of the intracellular pipette solution was the following (in mM): K-gluconate 138, 3 CsCl, 10 phosphocreatine, 4 ATP, 0.4 GTP, 10 HEPES, 0.2 QX-314. biocytin 3 mg/ml, adjusted to pH 7.3–7.35 using KOH (285–290 mOsm/L). Whole-cell series resistance was in the range of 5–15 MΩ. Both extracellular and whole-cell recordings were performed with a Multiclamp 700A or 700B amplifier (Molecular Devices). Voltage measurements were not corrected for the liquid junction potential. Both field and unit recordings were low-pass filtered at 3 kHz using the built-in Bessel filter of the amplifier. Data were digitized at 6 kHz with a PCI-6042E board (National Instruments) and recorded with EVAN 1.3 software (courtesy of Prof. I. Mody, University of California Los Angeles, Los Angeles, CA). All data were analyzed off-line using custom-made programs written in MATLAB 7.0.4 and Delphi 6.0 by AIG.

Local drug injections. Drugs were dissolved in HEPES based buffer (in mM; 126 NaCl, 10 Glucose, 2.5 KCl, 1.25 NaH2PO4, 2 CaCl2, 2 MgCl2, 26 HEPES, pH 7.3) containing phenol-red to visualize the spread of the solution injected. Control injections were made with the solution without drugs (n=5), and no effects were detected on the examined SWR parameters [sharp wave amplitude, p=0.81; ripple amplitude, p=0.63; ripple cycle count, p= 0.62; multi-unit count during SWR, p=0.42; SWR rate, p=1; Wilcoxon signed-rank test]. The amount of drug injected was controlled by the duration of mouth-applied pressure (from 10 sec to 1 min). To validate that local drug injection has no effect on global network behavior, an additional electrode (marked as control channel in Figure 3) was placed next to the "puffing channel" (at ~150 μm distance). After drug injection, SWR parameters on control channel showed no significant differences compared to baseline period [for example in case of agatoxin; n=7; sharp wave amplitude; p=0.63; ripple amplitude, p=0.63; ripple cycle count, p=0.62; multi-unit count during SWR, p=0.42; SWR rate, p=1; Wilcoxon signed-rank test).

To check for agatoxin effects other than blocking perisomatic inhibitory transmission, we puffed the drug onto PCs recorded in whole cell mode, while inhibition was blocked. No change in the membrane potential was observed (n=5; p=0.89, Wilcoxon signed-ranked test).

Recording of field potentials, cellular firing and drug effects. LFP and loose-patch recordings in one or two channel configuration were performed with ACSF filled standard patch pipettes (3-6 MΩ). An additional pipette was used to inject drugs within 20 μm from one of the recording electrodes during local drug injection experiments (presented in Figures 2-4.). Multiunits (MU) were detected as negative deflections larger than 3 standard deviations and duration of 0.05-1.5 ms in the 400Hz high-pass filtered signal.

Anatomical identification. The recorded cells were filled with biocytin. After the recording the slices were fixed in 4 % paraformaldehyde in 0.1 M phosphate buffer (PB; pH=7.4) for at least 3 hours, followed by washout with PB several times. Then sections were blocked with normal goat serum (NGS, 10%) diluted in Tris-buffered saline (TBS), pH 7.4, followed by incubations in Alexa-488 conjugated streptavidin (Molecular Probes, Vienna, Austria, 1:3000). Sections were then mounted on slides in Vectashield (Vector Laboratories) and were morphologically identified on the basis of their dendritic and axonal arborization. To distinguish basket cells and axo-axonic cells, slices were re-sliced to 40- μm-thick sections and processed for immunofluorescence double labeling. Ankyrin G-immunostaining was applied together with biocytin visualization as described before (Gulyas et al., 2010).

For camera lucida reconstruction of some representative cells after fluorescent examination, neurons were visualized using avidin-biotinylated horseradish peroxidase complex reaction (ABC; Vector Laboratories) with nickel intensified with 3-3-diaminobenzidine tetrahydrochloride (0.05% solution in Tris buffer, pH 7.4; Sigma) as a chromogen giving a dark reaction product. Then slices were dehydrated and embedded in Drucupan (Fluka) and cells were reconstructed using a drawing tube.

Immunostaining for Parvalbumin in ChR2-PV Mice. After recording slices were immediately transferred to fixative containing 4% paraformaldehyde (TAAB, UK) in 0.1 M phosphate buffer (PB) and fixed overnight. Following fixation slices were washed thoroughly in 0.1 M PB and were resectioned to 40 μm thick sections. After washing several times slices were transferred to a solution containing 10% normal goat serum (NGS) and 0.5% Triton X-100 in 0.1 M PB, followed by incubation overnight in a mixture of rabbit anti-parvalbumin (1:2000, Swant, Marly, Switzerland; Swant Cat# 235 RRID:AB_10000343) diluted in 0.1 M PB containing 5% NGS, 5% NHS and 0.5% Triton X-100. Following several washes in 0.1 M PB, the sections were treated with Cy3-conjugated donkey anti-rabbit secondary antibody (1:400; Jackson ImmunoResearch Labs Cat# 711-166-152 RRID: AB_2307437). After several washes, sections were mounted on slides in Vectashield. Maximum intensity z-projection images were taken using an A1R confocal laser scanning microscope (Nikon Europe, Amsterdam, The Netherlands) using a 60× (NA = 1.4) objective. We quantified the accuracy of ChR2 expression in PV-positive neurons by counting the number of cells expressing the two signals in the hippocampal CA3 area of 3 animals. We found that 87.7% (256 of 292 cells) of PV cells

expressed ChR2 in their membranes, but never saw ChR2 expressing elements without PV immunoreactivity.

Drugs. All salts and drugs were obtained from Sigma-Aldrich, except gabazine which were purchased from Tocris Bioscience, and ω-conotoxin and ω-agatoxin which were purchased from Almone labs.

Digital signal processing and analysis. Signals were filtered with a two-way RC filter to reserve phase. All automatic detection steps were supervised. Spike detection in loose-patch recordings was done on 500 Hz high-pass-filtered traces using a threshold value of six times the SD of the signal. SWRs were pre-detected on 30 Hz low-pass-filtered field recordings using a threshold value of four times the SD of the signal. The pre-detected SWRs were then re-detected using a program that measured various SWR features and eliminated recording artefacts similar to SWRs. Namely, on the low-pass-filtered signal the program measured: (1) peak amplitude and peak time of sharp waves, (2) duration of the sharp wave positive phase crossing 3 times SD, (3) amplitude, time, and half decay of the negativity following the SWRs. On a ripple band-pass-filtered trace (180– 200 Hz) the program also detected (4) the time of ripple negative peaks and taking the absolute value of the ripple band-passed signal and low- pass filtering it calculated (5) the ripple power peak, time, and area. Ripple frequency was calculated by Fast Fourier transformation or by calculating the characteristic ripple negativity inter-event interval. We identified the ripple cycle closest to the SWR peak and used its negative peak as triggering event for averages and correlations to preserve ripple phase. Averages shown in Figure- 3-4; were calculated from 20-20 SWRs immediately before and after puff application of drugs. For the calculation of peri-stimulus time histograms shown in Figure 1, the start of postsynaptic currents (PSCs) was defined as the PSC event time. Averaged ripple cycles are shown in Figure 6 E to show the interaction between ripple cycle number and optical stimulation length. On the graph of Figure 6 F ripple cycle numbers were first detected in individual SWRs and then averaged to plot. Since it is easier to detect ripples on averaged traces than on individual SWRs, the number of ripple cycles is systematically higher in Figure 6-E than of corresponding points of the graph in Figure 6 F.

Online detection of SWRs: We used an Arduino UNO microcontroller board (http://arduino.cc) running a script (written by A.I.G.) that read the signal from the amplifier and when the amplitude of the LFP crossed a manually set value, it triggered the onset of laser illumination through a digital signal with a modifiable delay and length.

Modeling.

We used the following simple model to fit the inter-event- interval (IEI) distributions of SWRs. We assume that, following a given SWR event, the next SWR is generated when the number of PCs firing (c out of a total N) in a relevant time bin (the integration time of PCs, Δt) first exceeds a threshold value. We further assume that the threshold increases transiently after a SWR, and then decays back to its baseline value (n) following an exponential time course (with time constant τ). We aim to calculate the probability that the number of PCs firing within the integration time window first exceeds the threshold after a period t* following the previous SWR. This can be obtained as the probability that no threshold crossing occurred in any of the time bins before time t*, and that the threshold is crossed during the time bin at time t*. We assume that the firing of PCs can be approximated by independent Poisson processes (of rate r) between SWRs. For realistic values of r (less than 1 Hz) and Δt (at most a few tens of ms), the probability of a given PC firing more than one spike in a given time bin is vanishingly small, and the probability that it fires one spike is approximately r·Δt. Therefore, the total number of PC spikes in a time bin follows a binomial distribution with parameters N and r·Δt. The probability that the first threshold crossing occurs in the k'th time bin is then given by

$$P[IEI = k\,\Delta t] = \prod_{j=1}^{k-1} P[c_j < n_j] \cdot P[c_k \geq n_k]$$
$$= \prod_{j=1}^{k-1} cdf[binomial(n_j; p_j, N)] \cdot (1 - cdf[binomial(n_k; p_k, N)])$$

where ck is the actual number of active cells in the k'th bin, nk is the threshold at that time point, and pk is the probability of any one cell firing in that time bin. A continuous approximation to this formula is

$$P[IEI = t^*] = \frac{1}{\Delta t} e^{\frac{1}{\Delta t} \int_0^{t^* - \Delta t} dt \ln cdf[binomial(n(t); r(t)\Delta t, N)]}$$
$$\cdot (1 - cdf[binomial(n(t^*); r(t^*)\Delta t, N)])$$
$$= \frac{1}{\Delta t} e^{\frac{1}{\Delta t} \int_0^{t^* - \Delta t} dt \ln I_{1 - r(t)\Delta t}(N - n(t), n(t) + 1)}$$
$$\cdot (1 - I_{1 - r(t^*)\Delta t}(N - n(t^*), n(t^*) + 1))$$

where cdf stands for cumulative density function, and I is the incomplete beta function. Assuming that r(t)=r is constant, and n changes as

$$n(t) = n_0 \cdot \left(1 + q \cdot e^{-\frac{t}{\tau}}\right)$$

following a SWR at time 0, we fit the parameters r, Δt and τ concurrently for all experiments, and the parameters n0 and q individually for each experiment, using the nonlinear least-squares optimization function lsqnonlin of MATLAB (R2009b).

Model network of reciprocally connected CA3 PV+ basket cells.
Parvalbumin-containing basket cells (PVBCs) were modeled as single-compartment linear integrate-and-fire neurons. The parameters of the model cell were set such that the firing frequency vs. input current relation (f-I curve) of the model cell approximated closely the f-I curve of real CA3 PVBCs as measured by a series of step current injections during somatic whole-cell recordings (n=4) in the slice. The resulting parameters were the following: membrane resistance: 200 MOhm; membrane time constant: 14 ms; mean resting potential: -70 mV; action potential threshold: -50 mV; reset potential: -64 mV; absolute refractory period: 0.1 ms. The actual value of the resting potential varied from cell to cell according to a uniform distribution with standard deviation 2.5 mV to create heterogeneity among the PVBCs. We estimated based on published cell counts (Jinno and Kosaka, 2010) that the number of relatively intact PVBCs in the CA3 region of a 600 μm thick slice from the ventral hippocampus is around 150. We estimated the probability that a given PVBC establishes synaptic contact with another arbitrarily chosen PVBC in the slice to be about 0.15. Synaptic inputs were assumed to have an exponential time course (time constant: 1.5 ms), a delay of 1.5 ms, a reversal potential of -70 mV, and a maximal conductance of 2 nS (Bartos, 2002). Each PVBC received a step current injection of amplitude 400 pA, lasting for 50 ms. The simulation was implemented using the PyNN (Davison, 2008); RRID:nif-0000-23351) simulation package, and simulations were run using the NEST simulator (Gewaltig and Diesmann, 2007); RRID:nif-0000-00162).
Statistics. Throughout the manuscript we used median, 1st and 3rd quartiles for the description of data groups, because they usually did not show Gaussian distribution. In these cases, Wilcoxon's signed-rank test was used to test for statistically significant differences between groups. The application of other statistical tests is indicated in the text.

Results

A prolonged build-up of neuronal activity precedes ripple modulated firing during SWRs.

In our modified submerged slice chamber SWRs occur spontaneously in the CA3 region of hippocampal slices (Hájos et al., 2009, 2013). SWRs were routinely present in slices of 400 (in 60 of 72 slices) to 600 μm (55/61) thickness, occasionally, at a low rate, in 350 μm-thick slices (9/40), and were seen only exceptionally in 300 μm-thick (or thinner) slices (3/300), suggesting that SWR generation requires a minimum network size and/or connectivity. We recently characterized spontaneously occurring SWRs in vitro (Hájos et al., 2013), and showed that they are transient highly synchronous events which are distinct from pharmacologically induced epileptiform bursts (Karlocai et al., 2014).
To study the initiation of SWRs, we first examined how the activity of inhibitory and excitatory neurons evolves before, during and after a SWR (Figure 1). We reasoned that the distribution of excitatory and inhibitory postsynaptic currents (EPSCs and IPSCs) in relation to SWRs (Hájos et al., 2013) will reveal the evolution of excitatory and inhibitory neuronal activity. We constructed summed peri-stimulus time histograms of detected excitatory and inhibitory synaptic events. We found significant baseline excitatory activity between SWRs that was not accompanied by comparable inhibitory activity. Approximately 55 ms before the sharp wave peak the frequency of EPSCs and IPSCs started to increase almost simultaneously. For the next 35 ms, until 20 ms before the peak of the SWRs, the increase of both excitation and inhibition
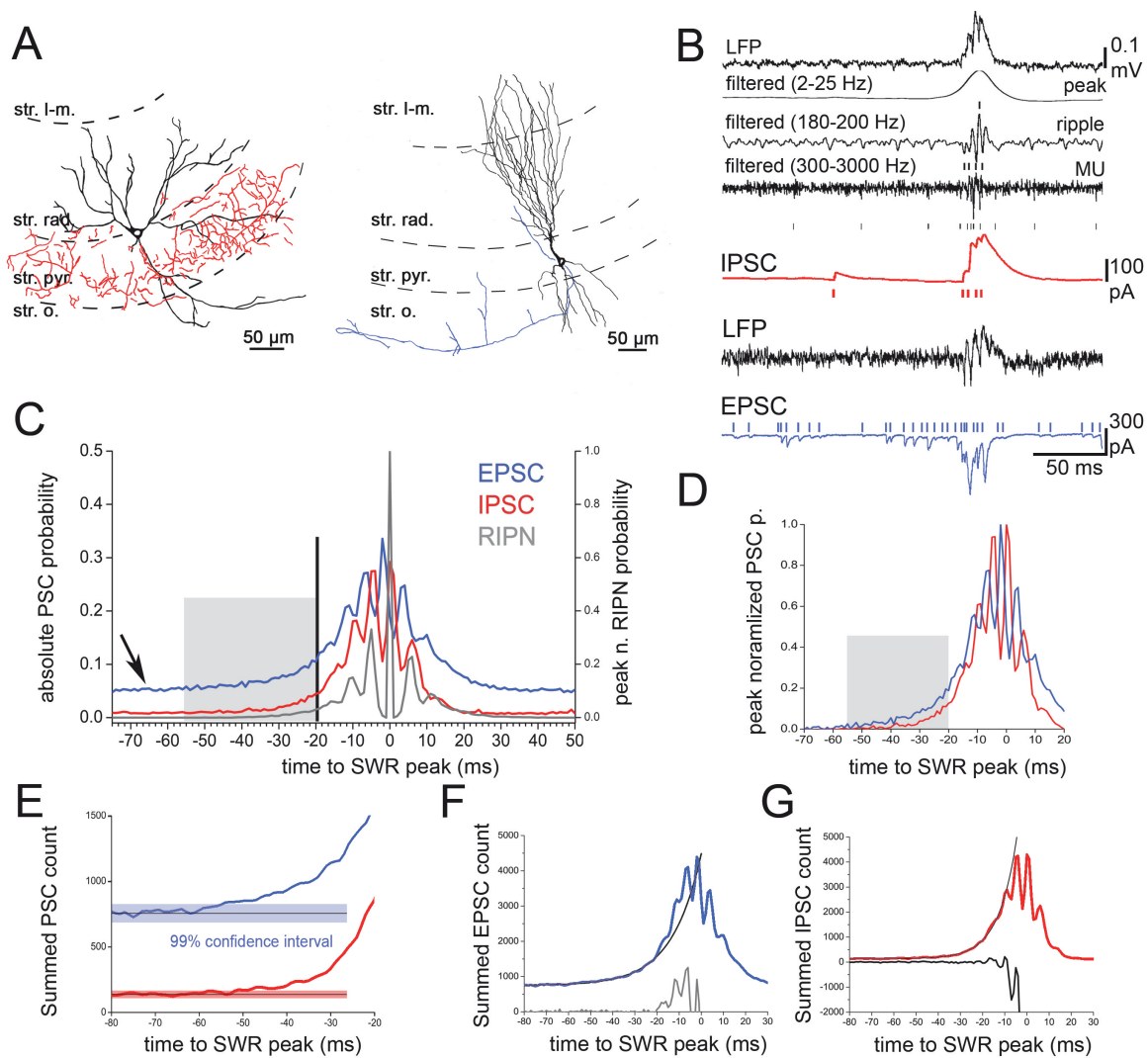
Figure 1. A gradual build-up of activity precedes ripple-modulated neuronal firing during SWRs.
A, Camera lucida reconstruction of a recorded parvalbumin-positive basket cell (PVBC, left) and a pyramidal cell (PC, right).
B, IPSCs and EPSCs were recorded from PCs and different subsets of interneurons (n=79) from the CA3 area during spontaneous sharp-wave ripple activity (SWR). Using the LFP (top trace) we automatically detected sharp wave peaks (using low-pass filtered traces, second trace), ripple negative peak times (band-pass filtered, third trace) and multi-units (high-pass filtered, fourth trace), together with IPSCs (fifth trace) or EPSCs (LFP and voltage clamp recording from another experiment). C, We then created peri-stimulus time histograms of EPSCs (blue), IPSCs (red) and ripple negativities (RIPN, light gray) around SWR peaks. Note that: 1) there is considerable baseline excitatory activity between SWRs (arrow), accompanied by a much smaller amount of inhibitory activity (p<0.001), 2) both excitatory and inhibitory activity start to increase ~55 ms before the SWR peak (grey box, significantly different from baseline at p=0.01 assuming independent samples from a Poisson distribution), closely follows an exponentially increasing curve until 20 ms before the SWR peak (p=0.01) and 3) ripple modulation of activity starts when the level of excitatory (and inhibitory) activity reaches a threshold (vertical line). D, Peak-normalized peri-stimulus time histograms of EPSCs and IPSCs showing the build-up of activity before the SWR peak. Note that EPSCs and IPSCs get out of phase when ripple modulation starts. E, Here we show at higher magnification the summed EPSC and IPSC number before a SWR starts. The net excitatory activity (blue) starts to deviate significantly (p=0.01) from its baseline value (749.4; 99% confidence interval (CI): 680; 821) 55 ms before the SWR peak. From this point, the number of EPSCs closely follows an exponential curve (F), staying within the corresponding 99% confidence interval until 20 ms before the SWR peak, where it becomes ripple modulated. The latter fact becomes clearly visible when the exponential curve is subtracted from the original EPSC distribution (bottom line). In the case of IPSCs (red) the baseline activity is lower (133.4; 99% CI: 105,164), and its starts to deviate significantly from baseline (p=0.01) somewhat later compared to EPSCs, 52 ms before the SWR peak (G). Ripple modulation starts similarly 20 ms before SWR peak (bottom).

closely followed an exponential curve. At this point, where activity was already several fold higher than baseline, both types of activity started to be modulated at ripple frequency, and excitatory and inhibitory
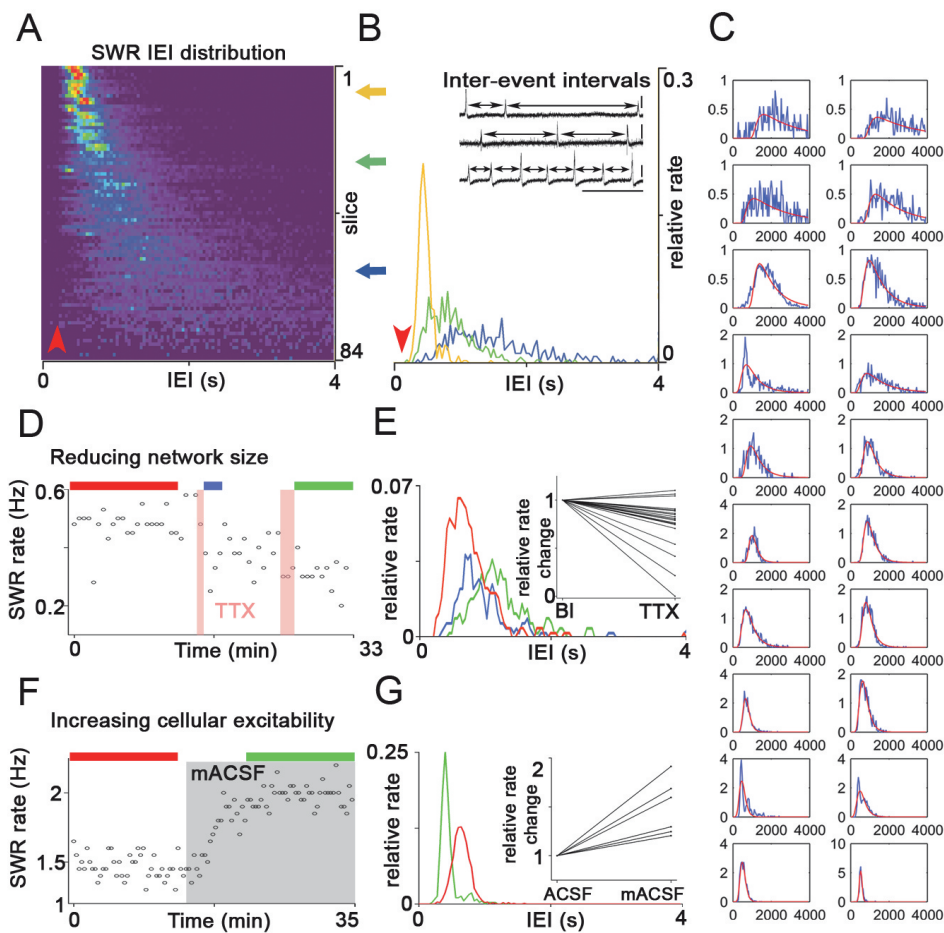
Figure 2. SWR initiation can be explained by a combined stochastic-refractory model.

A, Color-coded SWR inter-event interval (IEI) distributions from 84 slices (warm colors indicate high values). b) Three examples of SWR IEI distribution. Note that a universal gap (red arrowheads - A; B) occurs at short IEI lengths, which suggests some form of refractoriness following a SWR. C, Although the experimentally measured inter-event interval distributions (blue traces) show substantial variability across our experiments (n=84), all of these distributions can be fitted quite accurately using a simple mathematical model. The model assumes that, following a SWR event, the next SWR is initiated when a critical number of PCs fire within a fixed time window, and that this critical number transiently increases after a SWR due to a decrease in the efficacy of synaptic transmission and/or cellular excitability, and recovers exponentially with a given time constant. The fits in this figure (red curves) were obtained by assuming a PC population of 10,000 neurons, fitting a common coincidence detection window, PC activity level and recovery time constant for all experiments, and fitting the values of the threshold level of coincident firing and its relative change after an SWR individually for each experiment. The IEI distribution predicted by this model can be calculated explicitly, and is given in the Methods section. Only those experiments (68 out of 84) with at least 100 SWR IEIs shorter than 4 s were used for this analysis. 20 randomly selected examples are shown.

D, E, Puffing 1 µM TTX (the two vertical pink bars) into str. radiatum via a glass capillary (n=21) reduced SWR rate [E, inset; median, 0.66 (Hz) (1st quartile, 0.56; 3rd quartile, 0.98), and 0.53 (0.43; 0.95) in control conditions and after TTX application respectively; p<0.001; Wilcoxon signed-rank test], and increased IEI variability (red, blue, green horizontal bars indicate sampling period for distributions shown in E). F, G, Increasing cellular excitability by changing ACSF composition (modified ACSF, grey box, see methods, n=6) elevated SWR rate (G, inset; 1.18 Hz (0.63; 1.55) in control conditions, and 1.71 Hz (1.20; 1.87) after modified ACSF application, p=0.03, Wilcoxon signed-rank test), and decreased IEI variability (red, green horizontal bars indicate sampling period for distributions shown on G). Insets on E and G show normalized changes from all experiments.

events shifted 180 degrees out of phase. This threshold also coincided with the point where ripple modulation started to appear over the slow sharp wave envelope in the local field potential (LFP) signal.

Stochastic activity of PCs combined with a refractory mechanism initiate SWRs.

SWRs are irregularly occurring events, whose timing cannot be explained using a traditional oscillator model. Therefore, to examine what mechanism initiates the observed exponential build-up we detected SWRs and calculated their inter-event interval (IEI) distribution from 84 slices (Figure 2). The shape of the IEI distribution showed considerable variation across experiments, with many distributions (particularly those with larger means) having a long, approximately exponential tail at large IEIs, indicating a random component in SWR initiation. We also observed a universal gap at short IEI lengths (~200 ms) that suggests the presence of some refractory mechanism at network or cellular level.

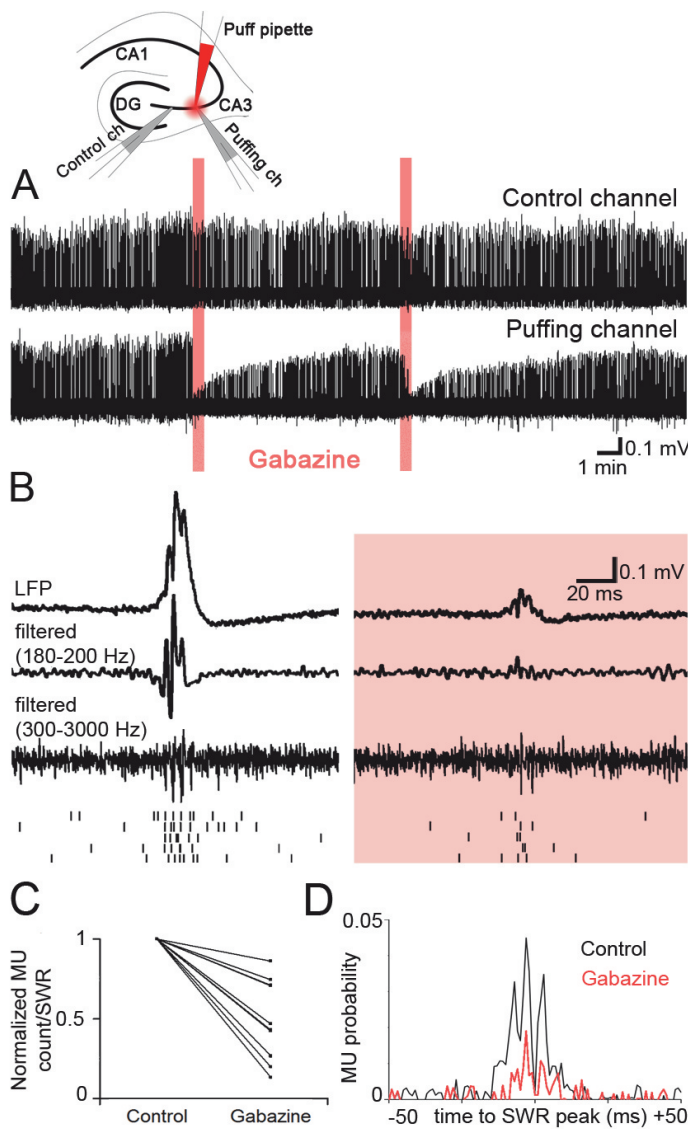Our results so far suggested the following working hypothesis: SWRs are initiated from randomly

Puff pipette

CA1

DG CA3

Control ch

Puffing ch

A

Control channel

Puffing channel

Gabazine

0.1 mV
1 min

B

LFP

filtered
(180-200 Hz)

filtered
(300-3000 Hz)

0.1 mV
20 ms

C

Normalized MU count/SWR

1

0.5

0

Control   Gabazine

D

0.05

MU probability

Control
Gabazine

0

-50   time to SWR peak (ms) +50

Figure 3. Perisomatic inhibitory currents are essential for the generation of the SWR LFP in str. pyramidale.
To examine the contribution of perisomatically evoked inhibitory currents to the SWR LFP, gabazine was locally puffed next to a recording electrode in str. pyramidale (experimental setup is shown on the top). A, There were no changes in global network activity as measured by the nearby (~100-150μm) control electrode (top). On the electrode (marked by "puffing channel") located close to the gabazine puff (n=8, 10 μM Gabazine), robust changes were detected. B, Averages (n=20) of SWR LFPs (top), traces filtered for ripple frequency (middle) and MUs (bottom) triggered by the SWR peak during baseline activity (left) and after the puff (right). At the bottom, raster plot of spikes are shown from consecutive SWRs. Following the gabazine puff, the amplitude of the SWR envelope (C) [5.17 mV (4.21; 6.71) in control and 2.81 mV (2.06; 4) after the application of gabazine] and the amplitude of ripple oscillations decreased strongly (ripple negative peaks were below the detection limit after gabazine puffs). The ripple phase-locked MUs vanished after the gabazine puff (D), and their frequency also decreased [5.17 (4.21; 6.71) vs. 2.81 (2.06; 4) MUs/SWR in control and after application of gabazine respectively, p<0.001].

fluctuating baseline activity when a sufficiently large number of PCs is active within a critical time window to initiate a build-up of activity in the recurrent excitatory network of CA3 PCs (de la Prida et al., 2006). We instantiated the above hypothesis in a simple mathematical model, and calculated the probability that the critical amount of coincident firing occurs first after a given time following the previous SWR. The model assumes that the amount of required coincidence increases temporarily after a SWR event (due to transient changes in synaptic transmission and/or cellular excitability), and then decays back to its baseline value with some time constant (see Materials and Methods). When we assumed that some parameters of the model (such as the threshold amount of coincident firing) may vary from experiment to experiment, while others (such as the baseline firing rate and the refractory time constant) are shared between all slices, we could fit all experimentally determined IEI distributions with distributions produced by the model very precisely (Figure 2C), supporting the validity of the model combining stochastic initiation with network refractoriness.

The stochastic element of the model predicts that the larger or more active the network is, the more frequent and regularly timed the SWRs are. The fact that SWRs were rarely observed in slices thinner than 350 μm is consistent with this prediction. We conducted two additional sets of experiments to test the predictions. In order to reduce functional network size, we locally injected a small amount of tetrodotoxin (TTX) into stratum radiatum via a glass capillary to block axonal conduction in some of the recurrent PC collaterals (Figure 2D-E). After application of TTX, the incidence of SWRs decreased significantly and the IEI distribution became wider. Conversely, when we slightly increased cellular excitability with a modified ACSF (mACSF; Figure 2F-G), SWR rate increased and the IEI distribution became narrower. These results support the validity of our model, and reinforce the presence of a stochastic element in SWR initiation.
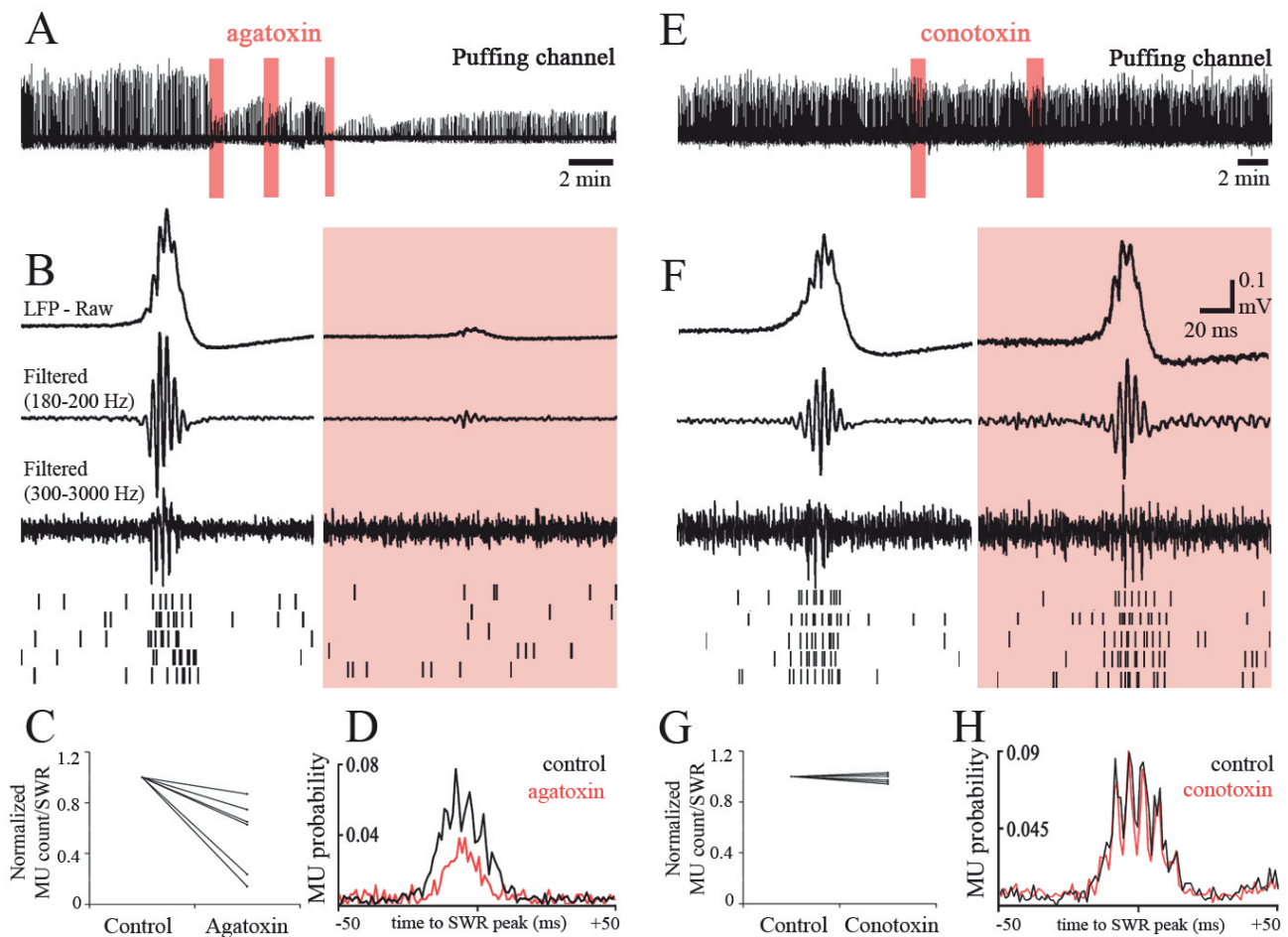
Figure 4. Perisomatic inhibition mediated by synapses utilizing P/Q-type voltage-gated Ca2+ channels is responsible for SWR generation and MU synchronization in str. pyramidale.

Puffing ω-agatoxin, a blocker of P/Q-type voltage-gated Ca2+ channels, produced similar effects to gabazine. A, LFP recordings from the channel where toxin was locally applied (red bars indicate the period of injections). Control channel is not shown (~100 μm distance, no changes, n=7). B, Averages (n=20) of SWRs during the baseline period (left) and after the puff (right; 1 μM ω-Agatoxin). Puffing ω-agatoxin also reduced SWR amplitude [0.54 mV (0.33; 0.56) in control and 0.15 mV (0.06; 0.25) after ω-agatoxin application; p=0.016; Wilcoxon signed-rank test], disrupted the ripple oscillation, and reduced the number [C; 7.05(6.05; 8.15) vs. 4.52(1.42; 5.62) MU events/SWR in control and after the puff, respectively; p=0.03] and phase-locking of MUs (D) similarly to gabazine. When we applied ω-conotoxin, a blocker of N-type voltage-gated Ca2+ channels (E, F, right; n=9), there were no changes in SWR parameters [SWR amplitude, ripple amplitude and ripple cycles p= 0.65; 0.74; 0.74 respectively; Wilcoxon signed-rank test], including MU rate (G) and synchrony (H).

Inhibitory currents mediated by PV+ cells contribute to the SWR local field potential and synchronize multi-unit activity in stratum pyramidale.

In order to identify the role of synaptic currents in the generation of the LFP and neuronal spiking in stratum pyramidale during sharp wave-ripples, we used a local injection of gabazine, a GABAA receptor antagonist, to eliminate perisomatic inhibition arriving onto PCs (Figure 3A-D). Excitatory inputs are not expected to contribute to str. pyramidale LFP, because no excitatory input arrives onto the perisomatic region of PCs (Megías et al., 2001).

Gabazine was injected via a glass capillary next to an extracellular recording electrode (marked as "puffing channel" in figures), and a control electrode was placed at ~150 μm distance to verify the local effect of the puff and to monitor network activity (experimental setup in Figure 3 top, see also Materials and Methods). At the location of drug application, SWR amplitude decreased nearly to zero, ripple oscillations vanished and, most importantly, the phase locking of multi-unit (MU) activity disappeared. Surprisingly, MU activity also decreased, suggesting that intact perisomatic inhibition may promote the firing of PCs during a SWR. The control electrode showed that the action of the drug was local and it did
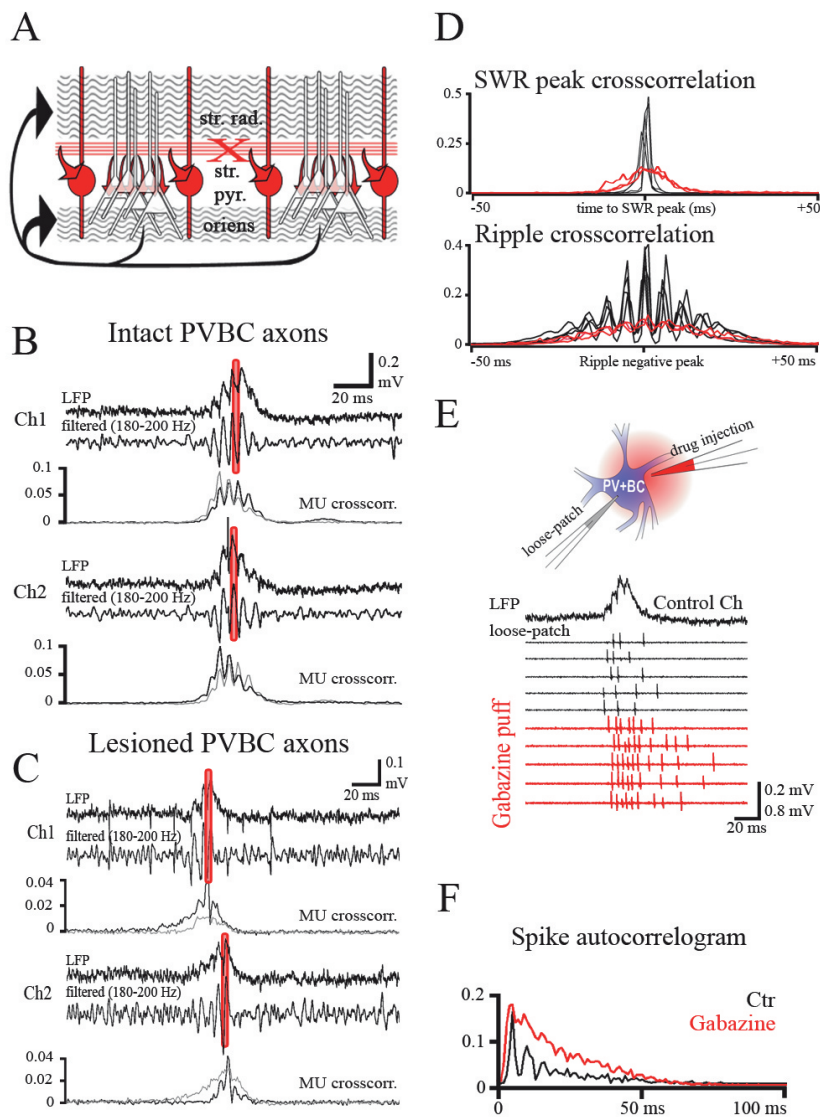
Figure 5. Cutting reciprocal connections between PV+ basket cells desynchronizes sharp waves and ripple oscillations

A, Outline of the experimental design. PV+ basket cells (PVBC) and their axons are shown in red, PCs and their recurrent collaterals in black. The red „X" marks the position of the cut at the border of strata pyramidale and lucidum, which separates the reciprocally connected PVBCs by cutting their axons, but leaves the recurrent collateral system of PCs, running in str. oriens and radiatum, intact. B and C, LFP recordings from two nearby (150 μm distance) sites in CA3 from a control slice (B, n=4) and from two halves of a cut slice (C, n=3). Both on Ch1 and Ch2 the unfiltered trace (top), the ripple-band filtered trace (middle) and the cross-correlation of SWR peak vs. MU activity (bottom) on the same channel (black) and on the opposite channel (gray) is shown. D, cross-correlation of sharp-wave peaks (top) and ripple negativities (bottom) in the control (black) and cut slices (red). Note the strong coupling between sharp wave peaks and ripple oscillations recorded concomitantly on the two electrodes in the control slice (B, black on D). Note that in the cut slice (C) SWRs are desynchronized (but remain close to each other) on the two channels (red cross-correlograms on top of D. Ripple oscillations are present in both halves, but they lose their coherence among the two halves (red on bottom of D). Also as shown by the black vs. grey SWR to MU cross-correlograms, in the cut slice MUs are correlated with the local, but not with the opposite SWR. E, PVBCs fire repetitive (3-5) action potentials locked to ripple oscillations under control conditions (PVBC in loose-patch configuration, black traces). Puffing gabazine onto their somatic region (n=6) and thus removing their inhibitory inputs eliminated the ripple phase-locking of the cell's firing (relative to the ripples detected on the control channel, black trace on the top), and, as expected from disinhibition, increased their firing frequency [grey; 3.09 (2.46; 4.11) and 5.3 (4.7; 6.08) spikes/SWR before and after puff application of gabazine, respectively; p=0.031, Wilcoxon signed-rank test]. F, The auto-correlogram of spikes demonstrates the loss of ripple modulation as a result of the removal of inhibition, suggesting that it is not the excitatory drive that phase-locks the firing of the cells.

not influence network behavior, because the incidence of SWRs and their measured characteristics did not change following the puff. Furthermore, no changes were detected on the control and puffing channels when drug free buffer solution was injected (see Materials and Methods).
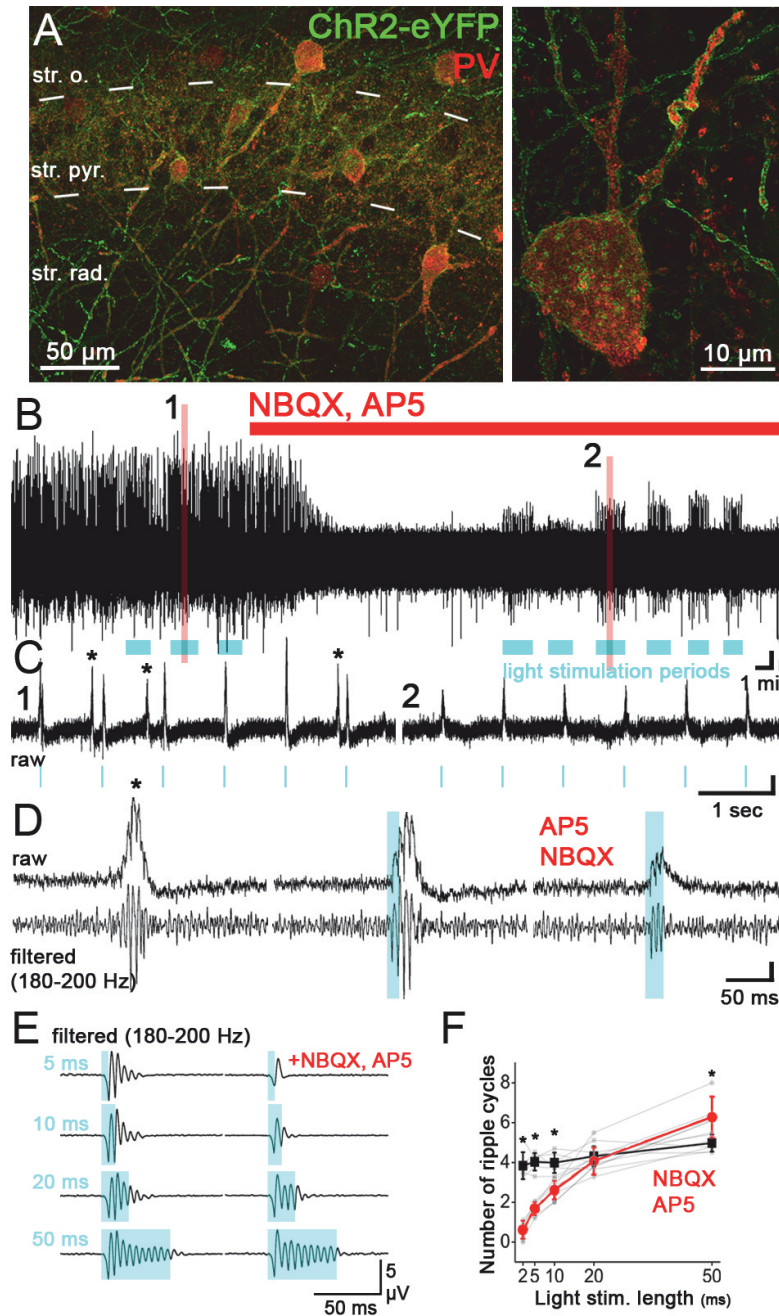
These results suggest that IPSCs contribute to the generation of the field potential signature of SWRs in stratum pyramidale, and, more importantly, perisomatic inhibition enforces ripple synchrony by phase-locking firing during SWRs.

To identify the type of neuron responsible for SWR-coupled perisomatic inhibition, we exploited the fact that the transmitter release of the two main classes of perisomatic region-targeting interneurons involves different voltage-dependent Ca2+ channels. Cholecystokinin-expressing basket cells express N-type Ca2+ channels at their axon terminals, which can be blocked by 500 nM ω-conotoxin, while parvalbumin-positive (PV+) basket (PVBCs) and axo-axonic cells have P/Q-type Ca2+ channels at their output synapses, which can be blocked by 500 nM ω-agatoxin (Wilson et al., 2001; Hefft and Jonas, 2005; Szabó et al., 2014).

When ω-agatoxin was injected locally into str. pyramidale (Figure 4A-D), we observed identical effects to

Figure 6. SWRs can be elicited by transient optogenetic driving of PV+ inhibitory neurons.

A, Immunofluorescent staining against parvalbumin (PV, red) in the CA3 area of animals expressing ChR2-eYFP (green) under the control of PV promoter shows that ChR2 is localized exclusively in the plasma membranes of PV-positive inhibitory neurons. B, Spontaneous and light-evoked (blue bars: stimulation periods) SWRs recorded from a slice in control conditions and with ionotropic excitatory transmission blocked (red bar). Note that spontaneous SWRs (s-SWR) disappear after the blockade of fast synaptic excitation (20 μM NBQX and 100 μM AP5; n=9). C, During the control period optogenetic stimulation of the PV+ cell population evoked SWRs between s-SWRs (asterisks, left) There was no significant difference between light evoked and spontaneous SWR parameters [sharp wave amplitude, p=0.63; ripple amplitude, p=0.81; ripple cycle number, p=0.82; SWR duration, p=1, Wilcoxon signed-rank test]. Following the blockade of fast excitatory synaptic transmission (right) sharp wave-like transients with ripple oscillations could still be evoked [ripple frequency189±16.7 Hz at light evoked, and 186±5.3 at spontaneous; p=0.62; paired t-test], albeit at a smaller amplitude [0.13 mV (0.11; 0.17) for spontaneous and 0.07 mV (0.06; 0.09] for evoked SWRs; p=0.016, Wilcoxon signed-rank test]. D, Examples of s-SWR (left), light-evoked SWR (middle), and light-evoked SWR during the blockade of fast excitatory synaptic transmission (right). E, SWR peak-triggered averages of stimulus-evoked ripple oscillations during spontaneous SWR activity (left) and during the blockade of AMPA and NMDA receptors (right). F, Correlation between the length of light stimulation and the number of evoked ripple cycles during baseline conditions (ACSF, black squares), and after blocking fast excitatory transmission (red squares; mean±standard deviation). Under baseline conditions any stimulation length shorter than the duration of spontaneous ripple duration evoked the same number of ripple cycles. Longer stimulation increased the number of ripple cycles to a small extent. The number of ripple oscillation cycles becomes the function of light stimulus duration in the absence of fast excitatory synaptic transmission.

those of GABAA receptor antagonist gabazine: the sharp wave amplitude decreased and the ripple oscillation vanished. Again, remarkably, the MU phase-locking disappeared and the MU frequency dropped. Intracellular recording of IPSCs and EPSCs showed that perisomatic application of agatoxin significantly reduced inhibitory currents, but had no effect on excitatory currents (not shown). This is agreement with the above quoted fact, that PCs receive no excitatory input onto their perisomatic region (Megias et al., 2001).

Local puffs of ω-conotoxin did not evoke any detectable change in SWR parameters (Figure 4E-H), indicating that cholecystokinin-expressing basket cells do not contribute to the generation of the SWR LFP or to MU phase locking. This is also supported by in vivo and in vitro data (Klausberger et al., 2005; Lasztóczi et al., 2011; Hájos et al., 2013) where this cell type was found to fire at low frequency during

SWRs and showed no or weak phase locking to ripple cycles.

By contrast, PV+ cells (especially PVBCs) were shown to fire phase-locked to the ripple oscillation during SWRs both in vivo and in vitro (Klausberger et al., 2003, 2005; Hájos et al., 2013). Our results indicate that PV+ cells are not just passive followers of the ripple oscillation, but their synaptic output contributes significantly to the field potential during SWRs, and is also essential for the phase-locking of MU activity.

Reciprocally connected PV+ basket cells generate ripple oscillation when driven by tonic excitation.

The next obvious question is how ripple phase-locked firing (Buzsáki et al., 2003) is generated. Gamma oscillations in the CA3 region are generated through the PING (pyramidal-interneuron gamma oscillation) mechanism (Whittington et al., 2000; Mann et al., 2004), which involves reciprocal interactions between PCs and PV+ cells. However, theoretical studies strongly suggest that this mechanism cannot operate at ripple frequency (Brunel and Wang, 2003; Geisler et al., 2005). Modeling studies (Perkel and Mulloney, 1974; Brunel and Wang, 2003; Taxidis et al., 2012; Schomburg et al., 2012) suggest an alternative mechanism, whereby a mutually interconnected network of inhibitory cells driven by tonic excitation generates a high-frequency coherent oscillation. We will refer to rhythms generated through this mechanism as Fast Inhibitory Neuronal Oscillation (FINO).

PVBCs, but not axo-axonic cells form mutually interconnected inhibitory networks in the hippocampus (Fukuda et al., 1996; Bartos, 2002). This fact, along with our observations that ripple oscillations start when the excitatory drive is sufficiently high (20 ms before SWR peak), and that ripple oscillations disappear when the output synapses of PV+ cells are blocked, suggests the following hypothesis. The tonic excitatory "envelope" arising from the build-up of activity of PCs drives the firing of PV+ cells. The activity of PVBCs then synchronizes at ripple frequency through the FINO mechanism, and their phasic inhibitory effect on PC output leads to ripple phase-modulated firing.

To verify the predicted role of PVBCs in the genesis of the ripple oscillation, we took advantage of the fact that the main axons of PV+ cells run at the border of strata pyramidale and lucidum (Pawelzik et al., 2002; Tukker et al., 2013). A small vertical cut here creates two separate, but internally connected subnetworks of PV+ cells without severing the recurrent collaterals of the PCs (which run in strata oriens and radiatum (Sik et al., 1993; Wittner et al., 2007) and thus retains a single continuous subnetwork of PCs. The cut is expected to decouple oscillations in the two halves of the slice (Figure 5A-D). In control (uncut) slices there is a strong coupling between sharp-wave peaks and ripple negative peak times recorded by electrodes placed 150-200 μm apart in stratum pyramidale. Cutting the PV+ cell network into two halves between the two electrodes introduced a non-directional jitter into relative sharp-wave peak times, but preserved their features. SWRs in the two halves were never separated by more than 20-25 ms and always occurred in both halves. The most striking result was that, while the ripple field oscillations and MU phase locking were intact in both halves, the ripples (Figure 5D) and, more remarkably, MU activity became massively uncorrelated between the two channels (Figure 5C), as demonstrated by the cross-correlograms.

These results revealed several key elements of the ripple generation mechanism. First, the tonic drive from the common excitatory build-up in the recurrent collateral system of the PCs drives the two PV+ cell sub-networks equally, but they start to generate ripple oscillations independently and ripples are not coherent in the two halves. Reciprocal connections between PV+ cells thus have an essential role in ripple generation and synchrony. Second, while neurons in the two halves are expected to receive a common excitatory envelop, they fire (as indicated by the MUs associated with the local ripples) only when the local PV+ cell network is engaged, further supporting the idea that phasic perisomatic inhibition is somehow important in making PCs fire during ripples. Finally, the experiments also suggest that the neuronal coupling via gap junctions is not essential in ripple synchronization, because these electrical
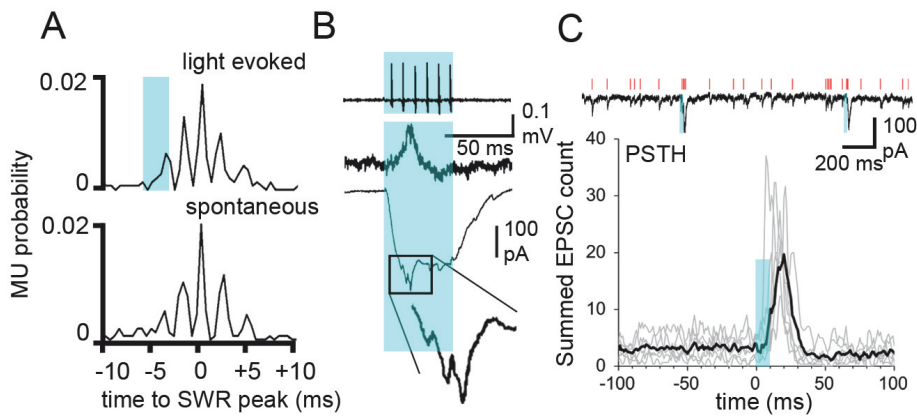
Figure 7. Depolarization of PVCs drives multi-units and evokes EPSCs.

(A) As shown in Figure 6D, optogenetic stimulation of PVCs evokes SWRs similar to spontaneous ones. As shown by the cross-correlations between SWR peaks and MU activity a 5 ms stimulation of PVCs generates MU distributions which are similar to those of spontaneously occurring SWRs. B, Optogenetic driving of PVCs evoked SWRs and repetitive action potentials in PVCs recorded in loose-patch configuration (top two traces, n=2), as well as inward tonic currents (~290 pA) ornamented with phasic EPSCs in whole-cell voltage-clamp recordings (bottom trace and inset, n=2). C, Transient (10 ms) optogenetic activation of the PVC population evoked a barrage of EPSCs in PCs (top, PCs held at -75 mV). The increase in EPSC occurrence in response to illumination (blue marks) is shown on a peri-stimulus time histogram of detected EPSCs around the start of the stimulation (bottom, n=6; EPSC sums from 100 sweeps in 1 ms bins; average shown as the black trace). EPSC frequency significantly increased in response to the activation of PV+ inhibitory neurons [20.7 (15.4; 31.4) at baseline and 73.6 (71.2; 118.9) following illumination in Hz; p=0.03; Wilcoxon signed-rank test]. We never saw ChR2 mediated currents in PCs (n=13) that confirmed our anatomical data that there is no misexpression of ChR2 in CA3 PCs.

connections among PV+ cells are found not in str. pyramidale but further out in the basal and apical dendritic tufts (Fukuda and Kosaka, 2000), and thus they should have been preserved by the minor cut that desynchronized activity in the two halves of the cut slice.

To directly prove the role of reciprocal inhibition in phase-locking the firing of PV+ cells at the single cell level, gabazine was puffed onto the somata of post hoc identified PVBCs recorded in loose-patch configuration (Figure 5E-F). The puff increased the frequency of their SWR-associated firing and abolished its ripple modulation, confirming the importance of phasic inhibitory input in timing the firing of PVBCs in the ripple frequency range. This finding also argues against a critical role of gap junctions in the genesis of ripple oscillations, because gabazine eliminated ripple phase locking, yet it has not been reported to affect the function of gap junctions.

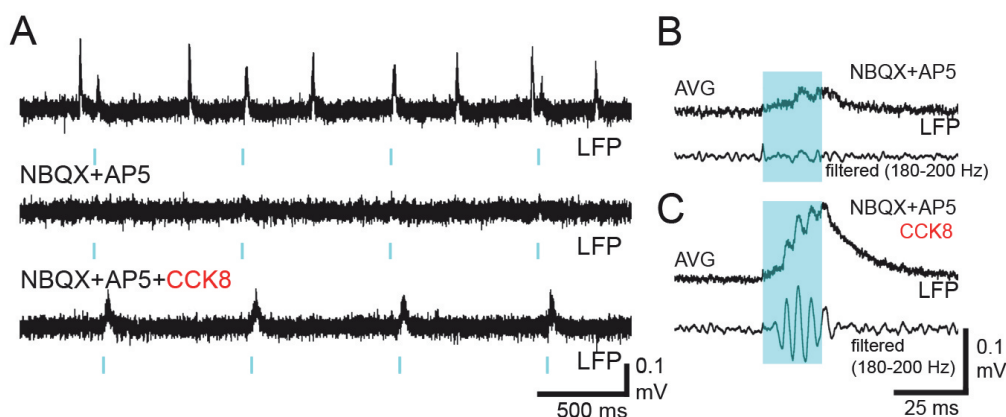**Optogenetic driving of PV+ inhibitory cells evokes sharp wave-ripples.**

Figure 8. Depolarization of PVCs with CCK8 facilitates optogenetically evoked SWRs after blockade of fast excitatory transmission.

A, LFP recordings showing optogenetic stimulation (blue marks, 20 ms) of PV cells during the baseline period (top), and after blockade of AMPA and NMDA receptors (middle, bottom). Note that a selective tonic depolarization of PV cells with CCK8 (bottom, 500 nM, n=4) assisted the optogenetic induction of SWR-like field potential transients in this experiment. Averages of evoked waveforms (60 events) before (B) and after (C) adding CCK8 to the bath solution, are shown.

To directly test the idea that selectively driving PV+ cells evokes high-frequency oscillation in the network, we used transgenic animals where the light-activated ion channel channelrhodopsin-2 was expressed exclusively in these types of interneurons (Figure 6A). Under control conditions, when spontaneous SWRs occurred in the slice, brief light stimulations of the PV+ cells triggered field potential transients identical to spontaneous SWRs (Figure 6B-F), irrespective of stimulation length (5 to 50 ms). The evoked events contained both the slow component sharp wave and its superimposed ripple oscillation in the same amplitude ratio and timing as spontaneous SWRs. We then eliminated the contribution of PCs by blocking AMPA and NMDA receptor-mediated fast excitatory synaptic transmission by applying NBQX and AP-5 in the bath. Following drug application, spontaneous SWR activity vanished, but light stimulation kept evoking field potential transients that had a slow sharp-wave-like envelope ornamented with ripple frequency oscillations. Under these conditions the number of ripple cycles depended on the length of illumination, and
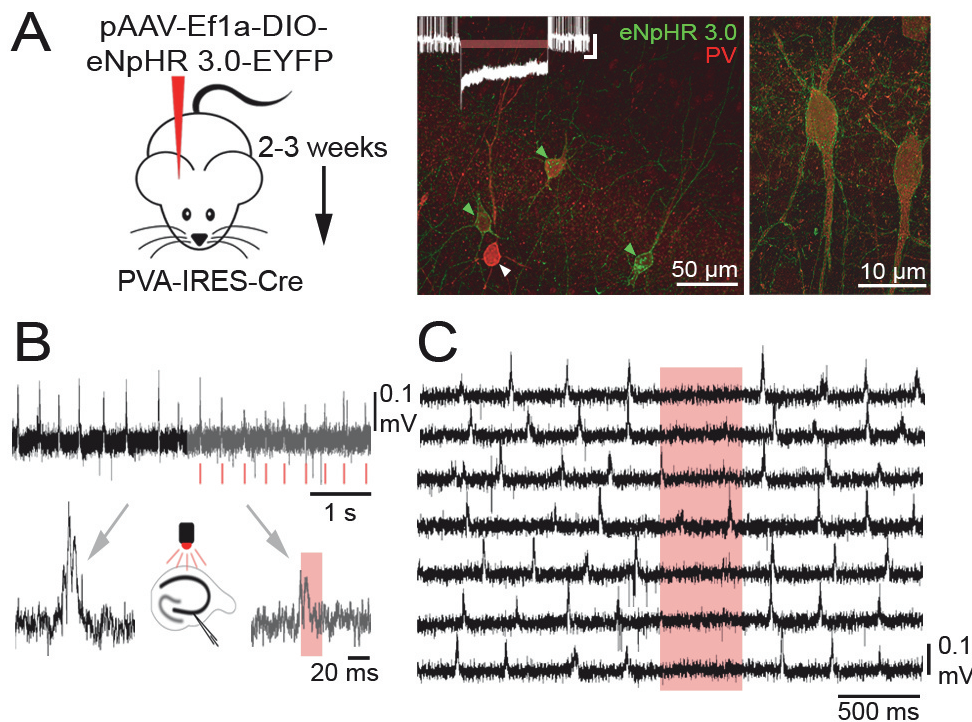

Figure 9. Silencing PV+ cells interrupts and blocks SWR generation

A, pAAV-Ef1a-DIO eNpHR 3.0-eYFP was injected into PVA-IRES-Cre animals to target PV+ cells in the hippocampal CA3 area (see Materials and Methods). B, Immunofluorescent staining against parvalbumin (PV, red) and eNpHR 3.0-eYFP (green) demonstrated that eNpHR 3.0 was localized exclusively in the plasma membranes of PV+ inhibitory neurons (green arrowheads). PV cells not expressing eNpHR 3.0 were also found (28.5%). On the insert, a PVBC is shown in current clamp configuration, which is effectively silenced in response to illumination (scale bars: 10 mV, 1s). C, Spontaneous SWRs were present in the hippocampal slices prepared after 2-3 weeks following virus injection (black traces). Transient laser illumination (red marks) triggered by the early phase of spontaneous, SWRs interrupted their further evolution (n=3, grey traces). The illumination significantly decreased ripple amplitude [61.53% (percentage of the baseline value); p=0.03; Wilcoxon signed-rank test], SWR length [56.78%; p=0.02; Wilcoxon signed-rank test] and the number of ripple cycles [50.3%; p=0.04; Wilcoxon signed-rank test]. D, Non-triggered, randomly timed, long (500 ms) illumination periods significantly reduced SWR initiation for the duration of the pulses (n=3, [30.6%; p=0.03; Wilcoxon signed-rank test]).

ripple oscillations could be maintained longer then the duration of spontaneous SWRs. The experiment demonstrates that a tonic excitatory drive can generate phasic inhibitory activity. The same observations were made in slices where the dentate gyrus had been removed (n=3), supporting the view that the CA3 network intrinsically generates SWRs.

The observation that (in the control case, but not when excitation is blocked) driving PV+ cells for even a short time initiates a full SWR, suggests that PV+ cell activation somehow engages the excitatory neurons, which then sustain the drive to PV+ cells, and a normal SWR is played out (see phase-locked MU spikes in Figure 7A). Indeed, when PV+ cells were driven by light pulses, a barrage of EPSCs could be recorded from either the PVBCs, superimposed on the light evoked inward current (~290 pA, n=4), or from PCs (n=13, Figure 7B and C).

One additional observation confirmed our hypothesis regarding the mechanism of ripple generation. In some slices light stimulation failed to evoke ripple oscillations when rapid excitatory transmission was
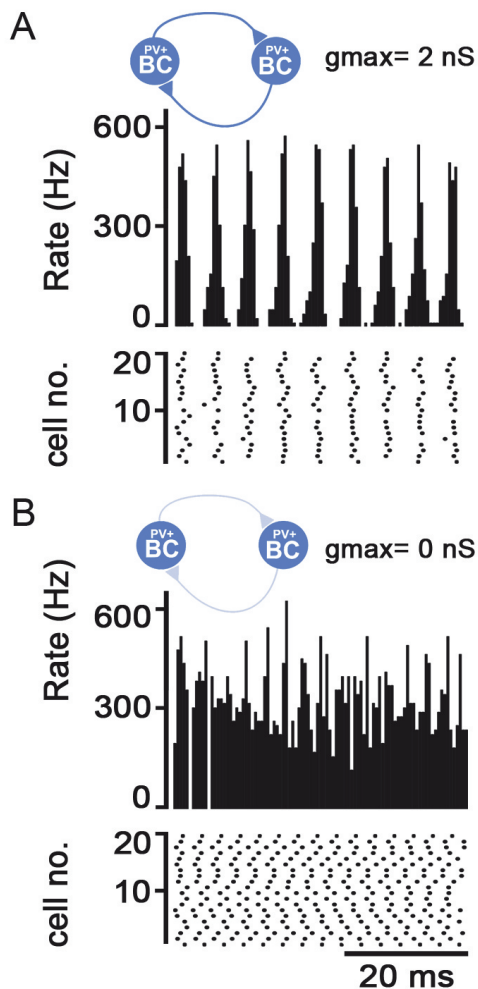
Figure 10. Network model of PVBC population generates ripple oscillation

A, Ripple frequency (approximately 180 Hz) phase-locked firing evolves in a model network of 150 reciprocally connected PVBCs when they are driven by a 400 pA depolarizing current step, mimicking a 50 ms-long light activation (top row). Firing rasters of a subset of model PVBCs are shown in the second row. B, When reciprocal inhibition is removed, the phase-locking of firing disappears and cells increase their firing frequency, similar to what happened in the experiment shown in Figure 5E-F.

blocked, probably because optical driving could not produce sufficient depolarization to drive high-frequency firing in PV+ cells. However, when we selectively depolarized PV+ cells with bath-applied CCK8 (Lee et al., 2011), SWR-like waveforms re-appeared in response to illumination (Figure 8A-C), strengthening the hypothesis that a tonic excitation of the mutually connected PV+ cells is sufficient to generate ripple frequency firing through the FINO mechanism.

Optogenetic silencing of PV+ inhibitory cells blocks sharp wave-ripples

To strengthen our claim for the role of PV+ cells in SWR generation, we tested the effect of temporarily silencing PV+ cells by optogenetic means under baseline conditions. eNpHR 3.0 was expressed in PV+ cells of the hippocampus following AAV-mediated Cre-dependent viral infection (Figure 9A; n=3 animals). The slices produced spontaneous SWRs, similar to the control animals. When on-line detected SWRs were used to trigger short laser pulses (640 nm; 20 ms), SWRs were interrupted, i.e. their amplitude, duration and ripple cycle count was significantly lower than that of control SWRs (Figure 9B). When we applied long light stimuli (500 ms) we could block the generation of SWRs. These experiments support our conclusions that PV+ cells are essential for the initiation and maintenance of sharp waves and the generation of ripple oscillations.

Model network of reciprocally connected CA3 PV+ basket cells generates rhythmic activity at ripple frequency

To further support the idea that a network of interacting PVBCs is responsible for the generation of ripple oscillations, we built a simple model of the PVBC network in area CA3 in our slice experiments (see Materials and Methods). The model neurons were stimulated by simultaneous step current injections, whose amplitude (which was varied in the range 200-500 pA) was determined using the conductance values measured in our earlier paper (Hájos et al., 2013), and also matches the values we measured in the optogenetic experiments. The model cells started to fire shortly after the beginning of the stimulus, and kept firing synchronously at high individual rates (Figure 10A), which varied in the range 60-260 Hz (depending on the magnitude of the driving current), for the duration of the input. By contrast, the frequency of the population oscillation remained stable (approximately 180-220 Hz) when the excitatory drive was varied. Synchronous firing at ripple frequency was due to inhibitory interactions between the cells, as eliminating these connections from the simulation resulted in asynchronous firing at an elevated rate (up to 300 Hz; Figure 10B), similar to what we observed in the gabazine puff experiment in Figure 5E. These results reinforce the idea that a reciprocally connected PVBC network, when its members are sufficiently excited, generates ripple oscillations in CA3.
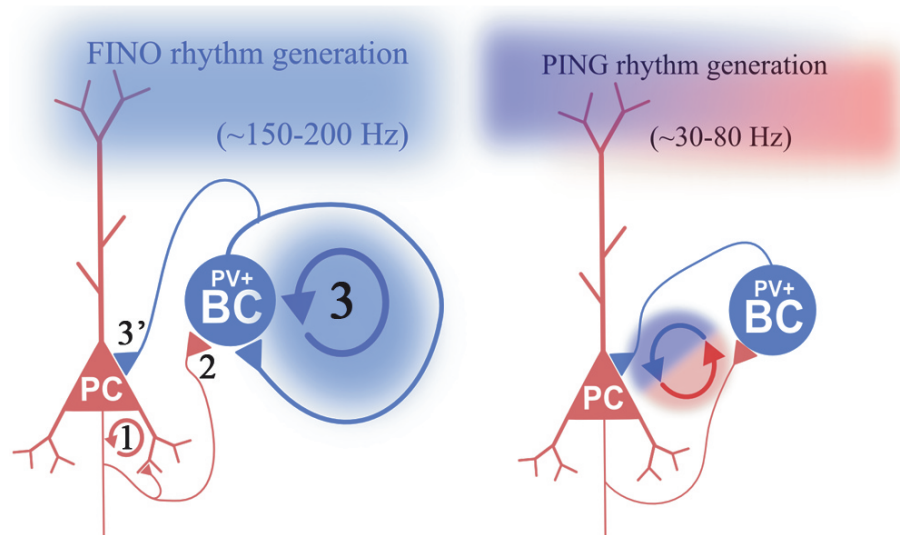
Figure 11. The mechanism of sharp wave-ripple complex generation and its comparison to the gamma generating PING mechanism

Left: Steps of SWR generation (1) Sharp waves are initiated stochastically due to the buildup of excitatory activity in the recurrent collateral system of the excitatory PCs (red). (2) The strong excitation starts to drive the firing of PVBCs (blue) and (3) their firing becomes ripple phase-locked and coherent due to their reciprocal inhibition. (3`) This ripple phase-locked inhibition is also fed towards the PCs and promotes their phase-modulated firing. Note that in the Fast Interneuron Oscillation (FINO) model there is no cycle-by-cycle reciprocal interaction between the PCs and the PVBCs. Right: in the Pyramidal-Inhibitory Network Gamma (PING) model, PC firing activates PVBCs that subsequently silence the PCs. When PCs recover from the inhibition, they begin to fire again and a new cycle starts. Note that here there is an alternation of excitatory and inhibitory activity due to the cycle-by-cycle interaction of PCs and PVBCs. The half a magnitude higher oscillation frequency is due to the facts that (a) IPSPs among PVBCs are faster than from PVBCs to PCs and (b) while in the FINO mechanism there is a single step cycle (blue circular arrow), there is a two-step cycle in the PING mechanism (Brunel and Wang, 2003; Geisler et al., 2005).

Discussion

Our results suggest the following model for the generation of SWRs in CA3 (Figure 11, left): First, a critical level of synchrony in PC firing, which is controlled by both stochastic and refractory mechanisms, initiates a buildup of activity in the recurrent excitatory collateral system of PCs. The resulting tonic excitation drives PVBC spiking. Their high-frequency firing is synchronized and phase-locked via reciprocal inhibition. Finally, this phasic activity of PVBCs phase-locks and, somewhat counter-intuitively, promotes (rather than inhibits) the otherwise tonic firing of PCs.

Stochastic and refractory mechanisms govern the initiation of SWRs
The following facts suggested a combined stochastic/refractory model for SWR initiation (see also (Peyrache, 2010)): 1) there is a baseline level of excitatory activity between SWRs; 2) activity starts to build up more than 50 ms before SWR peak (see also (Csicsvari et al., 2000); 3) there is characteristic gap in the distribution of inter-event intervals between subsequent SWRs. Similar ideas of activity buildup also emerged from earlier studies (Miles and Wong, 1983; Csicsvari et al., 2000; de la Prida et al., 2006), and we verified the hypothesis in subsequent experiments.
The presence of a refractory mechanism is an essential component of the model. It ensures that a SWR does not re-start within the observed 200-300 ms refractory window, and may also be responsible for the termination of SWRs. Various cellular and network level refractory processes can be listed as potential candidates, but several of these appear to be inconsistent with the observations. The firing of PCs accommodates due to the activation of adaptation currents; thus, as a SWR builds up, PCs may be less and less likely to fire.. Although we never observed PCs firing more than a single spike during SWRs, the slow buildup of depolarization or the occurrence of dendritic spikes could also reduce the responsiveness of PCs and help terminate SWRs even if the majority of PCs did not fire (Remy et al., 2009; Platkiewicz and Brette, 2011). Since PCs fire single spikes during SWRs the short-term depression of their terminals as a network level refractory mechanism is not an option either. SWRs could yet be terminated by an inhibitory neuron population that activates slowly during the elevated activity. However, in our recent study (Hájos

et al., 2013) we did not see interneurons activated during the second half of SWRs. A further candidate could be the short-term depression in the transmission of the repetitively firing PVCs (Galarreta and Hestrin, 1998; Kraushaar and Jonas, 2000)(Bartos et al., 2001).

Fast inhibitory neuronal oscillation (FINO) underlies ripple generation and phase locking of multiunit firing

Previous studies offer several hypotheses regarding the generation of high frequency oscillations. Some models propose coordinated burst firing of PCs (de la Prida et al., 2006; Foffani et al., 2007)(Jefferys et al., 2012), possibly synchronized via axonal gap junctions (Draguhn et al., 1998) or ephaptic entrainment (Anastassiou et al., 2010). Alternatively, fast oscillations may reflect the synchronized high-frequency firing of perisomatic region-targeting inhibitory interneurons (Buzsáki et al., 1992; Ylinen et al., 1995). Modeling studies (Perkel and Mulloney, 1974; Whittington et al., 1995; Wang and Buzsáki, 1996; Brunel and Wang, 2003; Taxidis et al., 2012) suggested a mechanism where a tonic excitatory drive generates a high-frequency coherent oscillation in a mutually interconnected network of inhibitory cells.

The somatic gabazine and agatoxin puff experiments revealed that eliminating perisomatic inhibition blocks ripple generation and eliminates MU phase locking, and thus support the last model above, which we refer to as Fast Inhibitory Neuronal Oscillation (FINO). This model is clearly different from the gamma generating PING mechanism (Figure 11, (Whittington et al., 2000; Mann et al., 2004), which involves phasic reciprocal interactions between PCs and PVBC cells, and cannot operate at ripple frequency (Brunel and Wang, 2003; Geisler et al., 2005). Our experiments and the neuronal network model also suggest that gap junctions are not essential components of the ripple-generating mechanism. While in the PING mechanism the activity of inhibitory neurons and PCs alternates, and inhibitory neurons fire at a relatively low frequency, our results show that in the FINO mechanism a strong tonic excitatory drive (that can be mimicked by optogenetic stimulation, Figures 6-8) evokes high-frequency firing in PVBCs, and their reciprocal inhibitory connectivity is essential for coherence (Figure 5). Thus, PVBCs are not only the current, but also the rhythm generators of the ripple oscillation (Figure 3).

The question why PVBCs inhibit PCs during gamma oscillations but only phase-lock PCs during SWRs can be resolved if we compare the results of the studies that measured synaptic input onto PCs during gamma oscillations (Hájos et al., 2004; Oren et al., 2006) and SWRs (Hájos et al., 2013). The comparison shows that while during gamma the ratio of the conductance of excitatory and inhibitory synaptic inputs onto PCs is 0.23, this ratio is twice as big during SWRs (0.47), suggesting a relatively stronger synaptic excitation of PCs during SWRs.

While our results pinpoint PVBCs (but not CCK+BCs) as critical components in the generation of ripple frequency firing, we could not address the role of axo-axonic cells in the absence of selective tools. As axo-axonic cells are not reciprocally connected (Somogyi, 1977), they cannot participate in the FINO mechanism. Nevertheless, they may amplify the rhythm of PVBCs, and participate in the selection of the subpopulation of PCs that start firing at the beginning of the SWR (Ellender et al., 2010). It is important to note, however, that they fire only in the first half of the ripple period (Klausberger et al., 2003; Hájos et al., 2013).

Although interneuronal synchronization through the FINO mechanism proved to be both necessary and sufficient for ripple generation, other resonance mechanisms, such as PC bursting or gap junctional coupling, may amplify and tune the oscillation.

Control of firing of MUs: Phase-locking and excitation by inhibition?

We have several matching observations suggesting that perisomatic inhibition, rather than inhibiting it, phase-locks and promotes MU firing during SWRs. Blocking perisomatic inhibition decreased MU frequency. When we separated the PVBC network into two halves, MU firing was associated with the local ripple oscillation and not with the common excitatory envelope, showing that local PVBC activity controls (phase-locks and promotes) MU firing in the given half. PV+ cells may also play a role in the initiation of SWRs as even a short (5 ms) optogenetic excitation of PV+ cells evoked a full SWR, associated MU firing and EPSC sequences, suggesting that activation of PVBCs engages the PCs.

As our recording configuration does not allow us to infer the types of cells contributing to MU activity, the contribution of PCs and different types of inhibitory cells to phase-locked MUs must be inferred indirectly. Though PCs are numerous, they fire rarely, while inhibitory neurons in str. pyramidale are in minority (3-4% of neurons), but are more active (especially PVBCs). Thus, in principle, both populations could contribute equally. However, the experiment shown in Figure 5E reveals that PVBCs increase their SWR-related firing following the elimination of perisomatic inhibition, while the observed MU frequency drops at the same time. This suggests that the MUs we observe derive mostly from PCs (as other subpopulations of inhibitory cells fire much less than PVBCs, see (Hájos et al., 2013)).

But how can perisomatic inhibition facilitate PC firing? There are several possible mechanisms: PV+ cells have been shown to inhibit dendritically projecting inhibitory neurons (Cobb et al., 1997). Therefore, when we eliminate perisomatic inhibition exerted by PV+ cells, dendritic inhibitory neurons will be disinhibited and that might cause a drop in the firing of PCs (Lovett-Barron et al., 2012). Alternatively, phase-locked perisomatic IPSPs could facilitate the firing of PCs during SWRs. One evident mechanism of excitation by inhibition is rebound firing (Cobb et al., 1995). However, this scenario is not supported by experimental evidence: we and other laboratories have never seen rebound firing in CA3 PCs (Ellender et al., 2010). A somewhat similar and more plausible mechanism is that IPSCs de-inactivate voltage-gated ion channels (primarily transient sodium channels (Platkiewicz and Brette, 2011)) inactivated by the slowly ramping excitation during the build-up phase, and help the cells fire phase-locked to ripples. The above mechanisms can even be synergistic. A more detailed examination of these possible mechanisms is necessary, but is beyond the scope of this study.

PVBCs have been shown to be key players in the PING mechanism, which generates cholinergically induced gamma oscillations in CA3 (Mann et al., 2005; Gulyas et al., 2010). Here, we show that the same interneurons are the necessary and sufficient elements of ripple generation, but are recruited into a different mechanism (see Figure 11). The mechanisms we revealed may also be applied to the transmission and generation of SWRs in CA1. The excitatory envelop in CA1 is transmitted via the Schaffer collaterals from CA3. Feed-forward excitation onto the local PVBCs that are also reciprocally connected may engage the FINO ripple generation locally, which could phase-lock CA1 PCs driven by excitation from CA3. Several studies noted earlier that the ripple frequency in CA1 versus CA3 is different (Buzsáki et al., 1992; Nádasdy et al., 1999; Sullivan et al., 2011; Tukker et al., 2013) and concluded that ripples must be generated locally. Our results provided a mechanism for local ripple generation. The fact that ripples of CA1 are not coherent with ripples of CA3 (Patel et al., 2013) also support that ripples are not transmitted from CA3 cycle by cycle, but are generated locally and thus rejects the PING model (where cycles are transmitted individually from CA3 to CA1 by phasic excitation, see (Zemankovics et al., 2013) and supports the FINO mechanism.

Author Contributions

A.I.G., D.S., N.H and T.F.F. conceived and designed the experiments. D.S.; A.I.G. and N.H. performed the experiments. A.I.G. designed analysis tools. D.S., S.K. and A.I.G analyzed the data. S.K. performed the mathematical modeling and simulations. D.S. and A.I.G. wrote the paper.

Competing Financial Interests
The authors declare no competing financial interests.

References

Anastassiou CA, Montgomery SM, Barahona M, Buzsáki G, Koch C (2010) The effect of spatially inhomogeneous extracellular electric fields on neurons. J. Neurosci. Off. J. Soc. Neurosci. 30:1925–1936

Bartos M (2002) Fast synaptic inhibition promotes synchronized gamma oscillations in hippocampal interneuron networks. Proc. Natl. Acad. Sci. 99:13222–13227 Available at: [Accessed September 2, 2013].

Bartos M, Vida I, Frotscher M, Geiger JR, Jonas P (2001) Rapid signaling at inhibitory synapses in a

dentate gyrus interneuron network. J. Neurosci. Off. J. Soc. Neurosci. 21:2687–2698

Brunel N, Wang X-J (2003) What determines the frequency of fast network oscillations with irregular neural discharges? I. Synaptic dynamics and excitation-inhibition balance. J. Neurophysiol. 90:415–430

Buzsáki G (1986) Hippocampal sharp waves: their origin and significance. Brain Res. 398:242–252

Buzsáki G (1989) Two-stage model of memory trace formation: a role for "noisy" brain states. Neuroscience 31:551–570

Buzsáki G, Buhl DL, Harris KD, Csicsvari J, Czéh B, Morozov A (2003) Hippocampal network patterns of activity in the mouse. Neuroscience 116:201–211

Buzsáki G, Chrobak JJ (1995) Temporal structure in spatially organized neuronal ensembles: a role for interneuronal networks. Curr. Opin. Neurobiol. 5:504–510

Buzsáki G, Horváth Z, Urioste R, Hetke J, Wise K (1992) High-frequency network oscillation in the hippocampus. Science 256:1025–1027

Buzsáki G, Leung LW, Vanderwolf CH (1983) Cellular bases of hippocampal EEG in the behaving rat. Brain Res. 287:139–171

Cobb SR, Buhl EH, Halasy K, Paulsen O, Somogyi P (1995) Synchronization of neuronal activity in hippocampus by individual GABAergic interneurons. Nature 378:75–78

Cobb SR, Halasy K, Vida I, Nyiri G, Tamás G, Buhl EH, Somogyi P (1997) Synaptic effects of identified interneurons innervating both interneurons and pyramidal cells in the rat hippocampus. Neuroscience 79:629–648

Csicsvari J, Hirase H, Mamiya A, Buzsáki G (2000) Ensemble patterns of hippocampal CA3-CA1 neurons during sharp wave-associated population events. Neuron 28:585–594

Davison AP (2008) PyNN: a common interface for neuronal network simulators. Front. Neuroinformatics 2 Available at: http://www.frontiersin.org/Journal/Abstract.aspx?s=752&name=neuroinformatics&ART_DOI=10.3389/neuro.11.011.2008 [Accessed November 22, 2013].

Diba K, Buzsáki G (2007) Forward and reverse hippocampal place-cell sequences during ripples. Nat. Neurosci. 10:1241–1242 Available at: [Accessed October 25, 2012].

Draguhn A, Traub R, Schmitz D, Jefferys J (1998) Electrical coupling underlies high-frequency oscillations in the hippocampus in vitro. Nature 394:189–192

Ellender TJ, Nissen W, Colgin LL, Mann EO, Paulsen O (2010) Priming of hippocampal population bursts by individual perisomatic-targeting interneurons. J. Neurosci. Off. J. Soc. Neurosci. 30:5979–5991

Foffani G, Uzcategui Y, Gal B, Menendez de la Prida L (2007) Reduced spike-timing reliability correlates with the emergence of fast ripples in the rat epileptic hippocampus. Neuron 55:930–941

Foster DJ, Wilson MA (2006) Reverse replay of behavioural sequences in hippocampal place cells during the awake state. Nature 440:680–683

Fukuda T, Aika Y, Heizmann CW, Kosaka T (1996) Dense GABAergic input on somata of parvalbumin-immunoreactive GABAergic neurons in the hippocampus of the mouse. Neurosci. Res. 26:181–194

Fukuda T, Kosaka T (2000) Gap junctions linking the dendritic network of GABAergic interneurons in the hippocampus. J. Neurosci. Off. J. Soc. Neurosci. 20:1519–1528

Galarreta M, Hestrin S (1998) Frequency-dependent synaptic depression and the balance of excitation and inhibition in the neocortex. Nat. Neurosci. 1:587–594

Geisler C, Brunel N, Wang X-J (2005) Contributions of intrinsic membrane dynamics to fast network oscillations with irregular neuronal discharges. J. Neurophysiol. 94:4344–4361

Gewaltig M-O, Diesmann M (2007) NEST (NEural Simulation Tool). Scholarpedia 2:1430 Available at: [Accessed November 22, 2013].

Girardeau G, Benchenane K, Wiener S, Buzsáki G, Zugaro M (2009) Selective suppression of hippocampal ripples impairs spatial memory. Nat. Neurosci. 12:1222–1223

Gulyas AI, Szabo GG, Ulbert I, Holderith N, Monyer H, Erdelyi F, Szabo G, Freund TF, Hajos N (2010) Parvalbumin-Containing Fast-Spiking Basket Cells Generate the Field Potential Oscillations Induced by Cholinergic Receptor Activation in the Hippocampus. J. Neurosci. 30:15134–15145 Available at: [Accessed October 25, 2012].

Hájos N, Ellender TJ, Zemankovics R, Mann EO, Exley R, Cragg SJ, Freund TF, Paulsen O (2009) Maintaining network activity in submerged hippocampal slices: importance of oxygen supply. Eur. J. Neurosci. 29:319–327 Available at: [Accessed October 25, 2012].

Hájos N, Karlócai MR, Németh B, Ulbert I, Monyer H, Szabó G, Erdélyi F, Freund TF, Gulyás AI (2013) Input-Output Features of Anatomically Identified CA3 Neurons during Hippocampal Sharp Wave/Ripple Oscillation In Vitro. J. Neurosci. Off. J. Soc. Neurosci. 33:11677–11691

Hájos N, Pálhalmi J, Mann EO, Nemeth B, Paulsen O, Freund TF (2004) Spike timing of distinct types of GABAergic interneuron during hippocampal gamma oscillations in vitro. J Neurosci 24:9127–37

Hefft S, Jonas P (2005) Asynchronous GABA release generates long-lasting inhibition at a hippocampal interneuron-principal neuron synapse. Nat. Neurosci. 8:1319–1328

Jefferys J, Menendez de la Prida L, Wendling F, Bragin A, Avoli M, Timofeev I, Lopes da Silva F (2012) Mechanisms of physiological and epileptic HFO generation. Prog. Neurobiol. 98:250–264

Jinno S, Kosaka T (2010) Stereological estimation of numerical densities of glutamatergic principal neurons in the mouse hippocampus. Hippocampus 20:829–840

Karlocai MR, Kohus Z, Kali S, Ulbert I, Szabo G, Mate Z, Freund TF, Gulyas AI (2014) Physiological sharp wave-ripples and interictal events in vitro: what's the difference? Brain Available at: http://www.brain.oxfordjournals.org/cgi/doi/10.1093/brain/awt348 [Accessed January 6, 2014].

Klausberger T, Magill PJ, Márton LF, Roberts JDB, Cobden PM, Buzsáki G, Somogyi P (2003) Brain-state- and cell-type-specific firing of hippocampal interneurons in vivo. Nature 421:844–848

Klausberger T, Marton L, O'Neill J, Huck J, Dalezios Y, Fuentealba P, Suen W, Papp E, Kaneko T, Watanabe M, Csicsvari J, Somogyi P (2005) Complementary roles of cholecystokinin- and parvalbumin-expressing GABAergic neurons in hippocampal network oscillations. J. Neurosci. Off. J. Soc. Neurosci. 25:9782–9793

Klausberger T, Márton LF, Baude A, Roberts JDB, Magill PJ, Somogyi P (2004) Spike timing of dendrite-targeting bistratified cells during hippocampal network oscillations in vivo. Nat. Neurosci. 7:41–47

Kraushaar U, Jonas P (2000) Efficacy and stability of quantal GABA release at a hippocampal interneuron–principal neuron synapse. J. Neurosci. 20:5594–5607 Available at: [Accessed September 26, 2013].

Lapray D, Lasztoczi B, Lagler M, Viney T, Katona L, Valenti O, Hartwich K, Borhegyi Z, Somogyi P, Klausberger T (2012) Behavior-dependent specialization of identified hippocampal interneurons. Nat. Neurosci. 15:1265–1271

Lasztóczi B, Tukker J, Somogyi P, Klausberger T (2011) Terminal field and firing selectivity of cholecystokinin-expressing interneurons in the hippocampal CA3 area. J. Neurosci. Off. J. Soc. Neurosci. 31:18073–18093

Lee SY, Foldy C, Szabadics J, Soltesz I (2011) Cell-Type-Specific CCK2 Receptor Signaling Underlies the Cholecystokinin-Mediated Selective Excitation of Hippocampal Parvalbumin-Positive Fast-Spiking Basket Cells. J. Neurosci. 31:10993–11002 Available at: [Accessed September 26, 2013].

Lovett-Barron M, Turi GF, Kaifosh P, Lee PH, Bolze F, Sun X-H, Nicoud J-F, Zemelman BV, Sternson SM, Losonczy A (2012) Regulation of neuronal input transformations by tunable dendritic inhibition. Nat. Neurosci. 15:423–430 Available at: [Accessed May 23, 2014].

Maier N, Nimmrich V, Draguhn A (2003) Cellular and network mechanisms underlying spontaneous sharp wave-ripple complexes in mouse hippocampal slices. J. Physiol. 550:873–887

Mann EO, Radcliffe CA, Paulsen O (2004) Hippocampal gamma-frequency oscillations: from interneurones to pyramidal cells, and back. J. Physiol. 562:55–63 Available at: [Accessed September 2, 2013].

Mann EO, Suckling JM, Hajos N, Greenfield SA, Paulsen O (2005) Perisomatic feedback inhibition underlies cholinergically induced fast network oscillations in the rat hippocampus in vitro. Neuron 45:105–117

Megías M, Emri Z, Freund TF, Gulyás AI (2001) Total number and distribution of inhibitory and excitatory synapses on hippocampal CA1 pyramidal cells. Neuroscience 102:527–540

Meyer AH, Katona I, Blatow M, Rozov A, Monyer H (2002) In vivo labeling of parvalbumin-positive

interneurons and analysis of electrical coupling in identified neurons. J. Neurosci. Off. J. Soc. Neurosci. 22:7055–7064

Miles R, Wong RK (1983) Single neurones can initiate synchronized population discharge in the hippocampus. Nature 306:371–373

Nádasdy Z, Hirase H, Czurkó A, Csicsvari J, Buzsáki G (1999) Replay and time compression of recurring spike sequences in the hippocampus. J. Neurosci. 19:9497–9507 Available at: [Accessed October 25, 2012].

Oren I, Mann EO, Paulsen O, Hajos N (2006) Synaptic currents in anatomically identified CA3 neurons during hippocampal gamma oscillations in vitro. J Neurosci 26:9923–34

Patel J, Schomburg EW, Berenyi A, Fujisawa S, Buzsaki G (2013) Local Generation and Propagation of Ripples along the Septotemporal Axis of the Hippocampus. J. Neurosci. 33:17029–17041 Available at: [Accessed May 23, 2014].

Pawelzik H, Hughes DI, Thomson AM (2002) Modulation of inhibitory autapses and synapses on rat CA1 interneurones by GABAa receptor ligands. J. Physiol. 546:701–716 Available at: [Accessed September 2, 2013].

Perkel DH, Mulloney B (1974) Motor pattern production in reciprocally inhibitory neurons exhibiting postinhibitory rebound. Science 185:181–183

Peyrache A (2010) Sequential reinstatement of neocortical activity during slow oscillations depends on cells' global activity. Front. Syst. Neurosci. 3 Available at: http://www.frontiersin.org/Journal/Abstract.aspx?s=1091&name=systems_neuroscience&ART_DOI=10.3389/neuro.06.018.2009 [Accessed September 26, 2013].

Platkiewicz J, Brette R (2011) Impact of fast sodium channel inactivation on spike threshold dynamics and synaptic integration. PLoS Comput. Biol. 7:e1001129

De la Prida L, Huberfeld G, Cohen I, Miles R (2006) Threshold behavior in the initiation of hippocampal population bursts. Neuron 49:131–142

Remy S, Csicsvari J, Beck H (2009) Activity-dependent control of neuronal output by local and global dendritic spike attenuation. Neuron 61:906–916

Schomburg EW, Anastassiou CA, Buzsaki G, Koch C (2012) The Spiking Component of Oscillatory Extracellular Potentials in the Rat Hippocampus. J. Neurosci. 32:11798–11811 Available at: [Accessed May 23, 2014].

Sik A, Tamamaki N, Freund TF (1993) Complete axon arborization of a single CA3 pyramidal cell in the rat hippocampus, and its relationship with postsynaptic parvalbumin-containing interneurons. Eur. J. Neurosci. 5:1719–1728

Somogyi P (1977) A specific "axo-axonal" interneuron in the visual cortex of the rat. Brain Res. 136:345–350

Sullivan D, Csicsvari J, Mizuseki K, Montgomery S, Diba K, Buzsáki G (2011) Relationships between hippocampal sharp waves, ripples, and fast gamma oscillation: influence of dentate and entorhinal cortical activity. J. Neurosci. Off. J. Soc. Neurosci. 31:8605–8616

Szabó GG, Nora Lenkey, Noemi Holderith, Tibor Andrási, Zoltan Nusser and Norbert Hájos (2014) Presynaptic calcium channel inhibition underlies CB1 cannabinoid receptor-mediated suppression of GABA release. J. Neurosci. in Press

Taxidis J, Coombes S, Mason R, Owen MR (2012) Modeling sharp wave-ripple complexes through a CA3-CA1 network model with chemical synapses. Hippocampus 22:995–1017 Available at: [Accessed May 23, 2014].

Tukker JJ, Lasztoczi B, Katona L, Roberts JDB, Pissadaki EK, Dalezios Y, Marton L, Zhang L, Klausberger T, Somogyi P (2013) Distinct Dendritic Arborization and In Vivo Firing Patterns of Parvalbumin-Expressing Basket Cells in the Hippocampal Area CA3. J. Neurosci. 33:6809–6825 Available at: [Accessed September 2, 2013].

Wang XJ, Buzsáki G (1996) Gamma oscillation by synaptic inhibition in a hippocampal interneuronal network model. J. Neurosci. Off. J. Soc. Neurosci. 16:6402–6413

Whittington MA, Traub RD, Jefferys JG (1995) Synchronized oscillations in interneuron networks driven

by metabotropic glutamate receptor activation. Nature 373:612–615

Whittington MA, Traub RD, Kopell N, Ermentrout B, Buhl EH (2000) Inhibition-based rhythms: experimental and mathematical observations on network dynamics. Int. J. Psychophysiol. Off. J. Int. Organ. Psychophysiol. 38:315–336

Wilson RI, Kunos G, Nicoll RA (2001) Presynaptic specificity of endocannabinoid signaling in the hippocampus. Neuron 31:453–462

Wiltgen BJ, Brown RAM, Talton LE, Silva AJ (2004) New circuits for old memories: the role of the neocortex in consolidation. Neuron 44:101–108

Wittner L, Henze DA, Záborszky L, Buzsáki G (2007) Three-dimensional reconstruction of the axon arbor of a CA3 pyramidal cell recorded and filled in vivo. Brain Struct. Funct. 212:75–83

Ylinen A, Bragin A, Nádasdy Z, Jandó G, Szabó I, Sik A, Buzsáki G (1995) Sharp wave-associated high-frequency oscillation (200 Hz) in the intact hippocampus: network and intracellular mechanisms. J. Neurosci. Off. J. Soc. Neurosci. 15:30–46

Zemankovics R, Veres JM, Oren I, Hajos N (2013) Feedforward Inhibition Underlies the Propagation of Cholinergically Induced Gamma Oscillations from Hippocampal CA3 to CA1. J. Neurosci. 33:12337–12351 Available at: [Accessed May 26, 2014].